HST Multicolor (255–1042 nm) Photometry of Saturn's Main Rings

I: Radial Profiles, Phase and Opening Angle Variations, and Regional Spectra

Jeffrey N. Cuzzi

Space Science Division, Ames Research Center, NASA, Mail Stop 245-3, Moffet Field, California 94035
E-mail: jcuzzi@mail.arc.nasa.gov

Richard G. French

Astronomy Department, Wellesley College, Wellesley, Massachusetts 02481

and

Luke Dones

Southwest Research Institute, 1050 Walnut Street, Suite 426, Boulder, Colorado 80302

The main rings of Saturn were observed with the Planetary Camera of the WFPC2 instrument on the Hubble Space Telescope (HST) from September 1996 to December 2000 as the ring opening angle to Earth and Sun increased from 4° to 24°, with a spread of phase angles between 0.3° and 6° at each opening angle. The rings were routinely observed in the five HST wideband UBVRI filters (F336W, F439W, F555W, F675W, and F814W) and occasionally in the F255W, F785LP, and F1042M filters. The emphasis in this series of papers will be on radial color (implying compositional) variations. In this first paper we describe the analysis technique and calibration procedure, note revisions in a previously published Voyager ring color data analysis, and present new results based on over 100 HST images.

In the 300–600 nm spectral range where the rings are red, the 555/336-nm ratio increases by about 14% as the phase angle increases from 0.3° to 6°. This effect, never reported previously for the rings, is significantly larger than the phase reddening which characterizes other icy objects, primarily because of the redness of the rings. However, there is no discernible tendency for color to vary with ring opening angle at a given phase angle, and there is no phase variation of color where the spectrum is flat. We infer from this combination of facts that multiple intraparticle scattering, either in a regolith or between facts of an unusually rough surface, is important in these geometries, but that multiple interparticle scattering in a vertically extended layer is not. Voyager color ratios at a phase angle of 14° are compatible with this trend, but calibration uncertainties prevent their use in quantitative modeling.

Overall ring average spectra are compatible with those of earlier work within calibration uncertainties, but ring spectra vary noticeably with region. We refine and subdivide the regions previously defined by others. The variation seen between radial profiles of ratios between different wavelengths suggests the presence of multiple compositional components with different radial distributions. We present new radial profiles of far-UV color ratio (F336W/F255W) showing substantial global variations having a different radial structure than seen between 555 and 336 nm. We constrain radial variation in the strength of a putative 850-nm spectral feature to be at the percent level or less. There seem to be real variations in the shape of regional ring spectra between 800 and 1000 nm.   © 2002 Elsevier Science (USA)

1. BACKGROUND

It has long been known that the material in Saturn's main rings is dominated by water ice (see, e.g., Lebofsky *et al.* 1970, Clark 1980, Esposito *et al.* 1984, Dones 1998). Water ice is far more stable than other common ices at 100 K (Pollack 1974), and its spectral features dominate the near infrared spectra of the rings (Clark 1980). However, the red spectrum of the rings between 300 and 600 nm clearly requires the presence of some additional non-icy material. Microwave radar and radiometry imply that the abundance of non-icy material mixed in with the ice is very small—certainly less than 10% by mass (Epstein *et al.* 1984), and possibly less than 1% (Grossman 1990, Clark 1980). This in itself is a real puzzle—how could the icy material have been so efficiently "distilled" away from other common rocky and/or carbonaceous materials? Pollack *et al.* (1973) suggested that the rings were primordial, with water ice condensing *in situ* after non-icy material had already condensed locally at higher temperatures and had been swept into the growing planet by gas drag.

However, current thinking is that the rings are in fact much younger than the Solar System. Part of this belief is based on dynamical arguments concerning the radial evolution of rings and close-in ring moons under resonant interactions (Goldreich and Tremaine 1982, Lissauer and Cuzzi 1985, Esposito 1987). An independent line of reasoning is based on meteoroid bombardment; this line itself has two parts. Pioneer 10 and 11 measurements of interplanetary micrometeoroid flux imply that Saturn's rings may have swept up their own mass in primitive, meteoritic material over the age of the Solar System (Morfill *et al.* 1983, Cuzzi and Durisen 1990, Cuzzi and Estrada 1998). This infall has been shown to have both structural effects matching observed structure which develop on a timescale of a few 10^8 years (Durisen *et al.* 1989, 1992) and, independently, compositional effects which match observed ring properties on a comparable timescale (Cuzzi and Estrada 1998) but violate observed properties if continuing over the age of the Solar System (Doyle *et al.* 1989). That is, it would be hard to reconcile the Pioneer fluxes with either the low microwave emission or the high visual albedo of the rings (Doyle *et al.* 1989). Meteoroid bombardment at these flux levels has been implicated as a causative factor in the "spokes" seen flickering across the rings (Goertz and Morfill 1983, Cuzzi and Durisen 1990) and in causing impact events in the F ring (Showalter 1998). However, see Dones (1998) for a different perspective on meteoroid fluxes.

The variation of the spectrum of the ring material with distance from Saturn carries clues as to the processes of meteoroid impact, deposition, and transport. Estrada and Cuzzi (1996) showed from limited (three-wavelength) Voyager imaging data that the color of the rings varies dramatically, not only on regional scales but on local radial scales of a few hundred kilometers. These variations are not easily explained by any likely particle size effect and probably represent compositional variation. Cuzzi and Estrada (1998) used the results, emphasizing green/UV (G/UV) filter reflectivity ratios, to assess the ring composition and its evolution with time under meteoroid bombardment. Cuzzi and Estrada (1998) found that meteoroid bombardment could explain not only the color ratios but also the form and shape of the radial variation across the inner edge of the B ring. They showed that likely silicates do not fit the spectral shapes of the non-icy components well, but radially varying fractions of organic "tholins" and carbonaceous compounds could. Subsequent ring color analysis was performed for the main rings by Poulet *et al.* (1999) using data from the Hubble Space Telescope (HST) archives. Their main ring data were obtained in 1991, with opening angles of around 20°, but using the original (aberrated) WF/PC, so they do not have the resolution of the data presented here. However, they obtained F555W/F336W color ratios which were smaller than the EC values over well-resolved regions.

The HST observations described in this paper are part of an ongoing systematic survey of Saturn's rings, begun just after the 1995–1996 ring plane crossing, when the rings were edge-on as seen from the Earth (Bosh and Rivkin 1996, Nicholson *et al.*

1996) and planned to continue until the rings reach their most open aspect, just prior to the arrival of the Cassini spacecraft at Saturn in 2004. Taking advantage of the diffraction-limited resolution and photometric precision of the WFPC2, this survey will eventually provide a uniform set of high-resolution Planetary Camera (PC) images of Saturn and its rings, spanning the full range of ring opening and solar phase angles visible from the Earth, over a broad range of wavelengths. Using the initial observations, we have begun to explore the opposition brightening of the rings (French *et al.* 1998b, Poulet *et al.* 2000, 2002), spokes in Saturn's B ring (French *et al.* 1998a), azimuthal brightness variations in the rings (French *et al.* 2000, Salo *et al.* 2000), and the peculiar orbital characteristics of Pandora and Prometheus, the two small satellites flanking Saturn's narrow F ring (French *et al.* 1998c, 1999; Dones *et al.* 1999).

Here, we focus our attention on the color of the rings, which we find varies not only with radial location within the main ring system, but also with changing illumination and viewing geometry, defined by the ring opening angle as seen from the Earth (B) and Sun (B') as well as the phase angle α. Our data set begins at a fairly low ring opening angle ($B = -4°$), but continues to larger opening angles, allowing good radial resolution to be obtained. Our observations were designed to separate geometrical effects (varying ring opening and phase angles) from intrinsic ring particle colors. In Section 2 we describe our observations and their reduction. In Section 3 we present the ring reflectivity profiles as functions of radius, and a series of radial profiles of color ratios (including several never previously observed); we also discuss their variation with phase and opening angles. Realizing that our HST results were consistent with those of Poulet *et al.* (1999) in being less red than Estrada and Cuzzi (1996), we reanalyzed and corrected the results of Estrada and Cuzzi (1996) (as discussed in Section 3.3, the calibration of Estrada and Cuzzi (1996) was incorrect, implying that the rings were redder than they actually are). In Section 4 we discuss the implications. In Section 5 we summarize our conclusions and pose a few questions and speculations.

2. HST OBSERVATIONS AND DATA REDUCTION

2.1. Observations

Table I summarizes the geometric characteristics of the HST observations used in this analysis and, for comparison, the corresponding values for the Voyager 2 data of Estrada and Cuzzi (1996). The five WFPC2 images in Fig. 1 illustrate the varying aspect of the rings over the range of ring opening and phase angles considered here. During each allocated HST orbit (or "visit") we obtained images of each ring ansa in the WFPC2 set of UBVRI filters (F336W, F439W, F555W, F675W, and F814W, respectively), and as time permitted, we extended the coverage to the UV and the near-IR by including occasional exposures using the F255W, F785LP, and F1042M filters. The

TABLE I
Observation Geometry

Spacecraft	Date	B (°)	B' (°)	α (°)
Voyager 2	August 23, 1981	13.7–13.2	8.01	14.1–14.9
HST	September 30, 1996	−4.31	−4.73	0.46
	October 14, 1996	−3.82	−4.93	1.93
	January 10, 1997	−3.72	−6.24	5.67
	September 22, 1997	−10.59	−10.01	2.00
	October 1, 1997	−10.28	−10.15	0.98
	October 6, 1997	−10.12	−10.22	0.50
	October 10, 1997	−9.99	−10.28	0.30
	January 1, 1998	−8.88	−11.47	6.02
	July 28, 1998	−16.67	−14.38	6.26
	October 13, 1998	−15.57	−15.42	1.20
	October 18, 1998	−15.43	−15.47	0.69
	October 24, 1998	−15.25	−15.56	0.32
	August 25, 1999	−21.05	−19.36	6.11
	November 3, 1999	−19.98	−20.16	0.43
	November 7, 1999	−19.90	−20.20	0.30
	August 4, 2000	−24.19	−22.92	6.10
	November 20, 2000	−23.56	−23.83	0.27
	November 24, 2000	−23.50	−23.85	0.59
	December 6, 2000	−23.33	−23.96	1.99

WFPC2 filter passbands used (after multiplication by the optics and detector responses) are shown in Fig. 2, along with similarly treated Voyager 2 filter passbands and a recent slit spectrum of the entire ring system (Karkoschka 1994) for comparison. On average, we have been allocated four HST orbits per Saturn opposition. Typically, we have devoted one of these to the highest phase angle accessible from Earth ($\alpha \simeq 6°$), and then sampled more densely at small phase angles to measure the sharp opposition brightening near zero phase. The reader who is not interested in the details of data calibration and reduction may wish to skip to Section 3.

2.2. Absolute Photometric Calibration

Standard photometric calibration of HST images, using the normal STScI pipeline processing, provides the average flux from the source over the range of sensitivity of the filter and detector. Because of the brightness of the rings, corrections for variable charge transfer efficiency across the chip were negligible, and we assumed that the standard flat field and bias corrections were satisfactory. However, the default flux calibration is not sufficient for Solar System targets. Since Saturn and the rings are illuminated by the Sun, we need to take into account the solar spectrum to determine the ring reflectivity from each image. The wavelength-dependent ring reflectivity, or I/F, is defined as the ratio of ring surface brightness I to that of a perfect, flat, Lambert surface at normal incidence $\pi F(\lambda)/\pi$, where $\pi F(\lambda)$ is the solar flux density or irradiance (erg cm^{-2} s^{-1} Å^{-1} at Saturn at wavelength λ). The conversion factor between data number (DN) in each pipeline-processed image and I/F is com-

puted in practice as

$$\frac{\text{DN}}{(I/F)} = \frac{\Omega A t_{\exp} f_{\text{decon}}}{D^2 G} \int_0^\infty \frac{F_\oplus(\lambda)\eta(\lambda)}{E(\lambda)} \, d\lambda, \quad (1)$$

where Ω is the solid angle (in steradians) subtended by a pixel (each PC pixel is 0.04554″ on a side—see Biretta (1996),
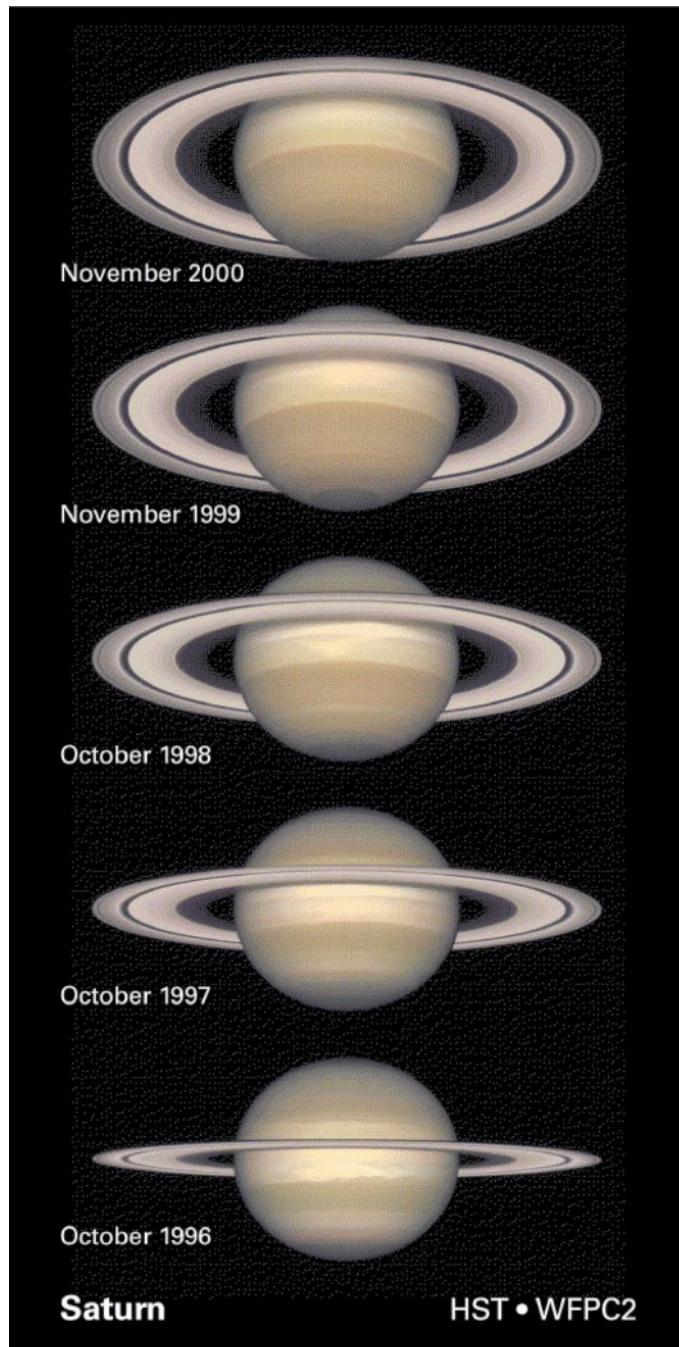

FIG. 1. HST Planetary Camera images (F555W); ring opening angle $B = -24°, -20°, -15°, -10°,$ and $-4°$. Image is courtesy of NASA, The Hubble Heritage Team (STScI/AURA), R. French (Wellesley College), J. Cuzzi (NASA/Ames), L. Dones (SwRI), and J. Lissauer (NASA/Ames).
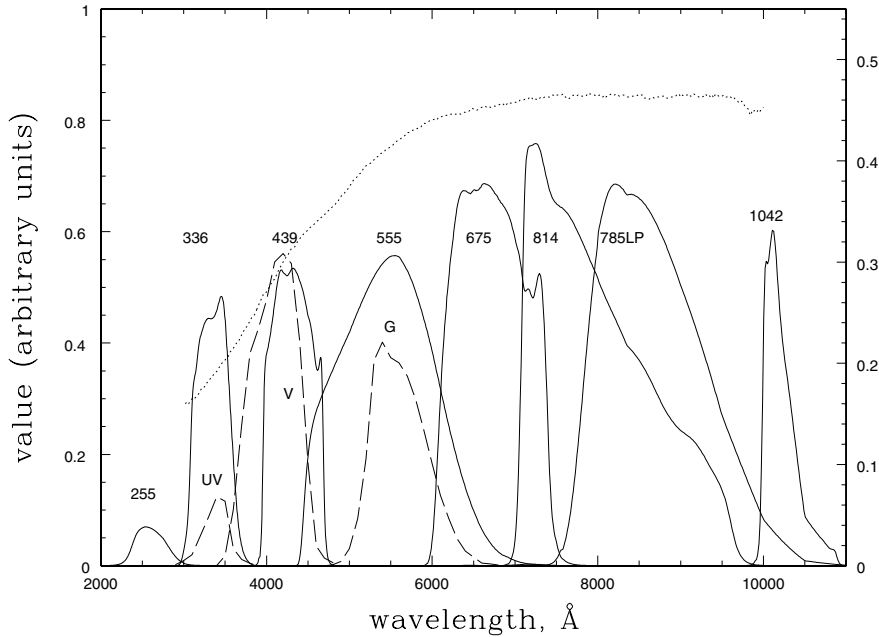
FIG. 2. HST and Voyager filter passbands (after multiplication by the optics and CCD response functions) are plotted on an arbitrary scale to show their wavelength correspondence. Voyager passbands are shown by the dashed curves, and HST passbands by solid curves. Note the good agreement between central wavelengths and widths for the HST F336W and F555W filters and the Voyager UV and G, respectively. Note from this figure and Table II that the passband for the long-pass filter F785LP has a longer effective wavelength ($\lambda_{\text{eff}} = 868$ nm) than the F814W passband ($\lambda_{\text{eff}} = 798$ nm). Also shown is a ring-average spectrum of reflectivity or I/F (right scale, Karkoschka 1994).

Section 5.10), A is the unobscured geometric area of the HST mirror, t_{exp} is the image exposure time (s), f_{decon} is the factor ($\lesssim 1$) by which the system throughput has decreased since the most recent decontamination of the optics (important only for the F255W and F336W images in our data set), D is the heliocentric distance to Saturn (AU), G is the gain of the detector in e^- per DN, $\pi F_{\oplus}(\lambda)$ is the solar irradiance at the Earth, $\eta(\lambda)$ is the detective quantum efficiency, or throughput of the filter, optics and detector in units of e^- per photon entering the unobscured 2.4-m telescope, and $E(\lambda) = hc/\lambda$ is the energy per photon, where h is Planck's constant and c is the speed of light.

We used the solar spectrum of Colina *et al.* (1996) to provide $\pi F_{\oplus}(\lambda)$ and obtained the most recent (June 1997) throughput files $\eta(\lambda)$ for each filter from the WFPC2 ftp site (`ftp://ftp.stsci.edu/cdbs/cdbs8/synphot_tables/`). The decontamination factors f_{decon} were computed by assuming a linear decrease with time of the F255W and F336W throughput corresponding to 0.00183 and 0.00062 per day, respectively (about 7% in 30 days for F255W), since the most recent decontamination of the optics (cf. Table 2 of Baggett and Gonzaga 1998). The decontamination times were obtained from `http://www.stsci.edu/instruments/wfpc2/Wfpc2_memos/wfpc2_decon_dates.html`. Table II summarizes the characteristics of the WFPC2 filters used in our analysis. For comparison with other WFPC2 observations, we include the predicted count rate (DN s^{-1}) from the PC for a solar-illuminated object at 1 AU with $I/F = 1$. These values are appropriate for the gain $G = 14/1.987 = 7.0458$ (nominally referred to as a gain state of 7—see Table 4.3 of Biretta (1996)) used for all of

our PC observations. We note in addition that the F336W filter has a red leak (Holtzman *et al.* 1995) which, for an object with the average color of the rings, leads to an F336W reflectivity which is 4% too high. In this paper, we scale each point in

TABLE II
WFPC2 Filter Characteristics

Filter name	$\lambda_{\text{eff}}{}^a$ (nm)	$\Delta\lambda^b$ (nm)	DN s^{-1} ^{c} (for $I/F = 1$, 1AU)	k^d
F255W	275	41	4.393×10^{2e}	-2.10
F336W	338^f	37	2.505×10^{4g}	-2.60
F439W	434	49	9.460×10^4	-2.75
F555W	549	122	8.217×10^5	-2.50
F675W	672	89	8.081×10^5	-2.40
F814W	798	176	6.953×10^5	-2.50
F785LP	868	210	3.159×10^5	-2.50
F1042M	1022	61	6.662×10^{3h}	—

^{a} Effective wavelength for solar illumination of white surface.

^{b} Approximate FWHM of filter (Table 3.1, WFPC2 Instrument Handbook, version 4.0 (Biretta 1996)).

^{c} For a gain of $14/1.987 = 7.046$ e^-DN^{-1}.

^{d} Power law index for PSF halo.

^{e} Does not include corrections for throughput losses due to contamination.

^{f} Uncorrected for red leak, which contributes about 4% to the total signal for an average Saturn ring spectrum.

^{g} Does not include corrections for throughput losses due to contamination.

^{h} The June 1997 STSCI throughput curve for filter F1042W was multiplied by 1.228, based on an analysis of calibration observations of white dwarf GRW + 70°5824 taken on February 8, 2000 as part of HST Observing Program 8451. See text for details.

each of our derived F336W I/F profiles by a radially varying correction function which depends on the local color of the rings to take this into account.

The calibration of the F1042M filter required special consideration. Using the June 1997 throughput file for this filter resulted in derived radial I/F profiles that were about 20% brighter than the F785LP and F814W profiles at nearby wavelengths. This sharp rise in the ring spectrum in the near-IR was at odds with ground-based observations (Karkoschka 1994; see Fig. 2), prompting us to investigate the F1042M calibration in more detail. Most of the WFPC2 filters have been calibrated using the white dwarf standard star GRW + 70°5824, and we examined the most recent set of such calibration images from HST Program 8451 (S. Baggett, principal investigator). We found that, for stellar (point source) photometry, the nominal F1042M throughput file was in error by about 10%, consistent with recent findings by S. Baggett (personal communication, 2001) based on the improved analysis of calibration observations since the initial calibration by Holtzman *et al.* (1995).

Furthermore, for extended objects such as the rings, an additional correction is required to convert from point source to surface brightness. By convention, the aperture correction to infinity from the standard 0.5″ radius aperture used for stellar photometry is *assumed* to be −0.10 mag (Casertano 1997). In the case of the F1042M filter, there is a substantial halo of scattered light, as discussed below in more detail, and much less than 90% of the starlight falls within a 0.5″ aperture. We predicted the total stellar signal for an infinite aperture for all of the February 8, 2000, PC images in HST Program 8541, using the June 1997 throughput files for each filter and an adopted absolute spectrum of the standard star provided by S. Baggett (personal communication, 2001). The high-resolution absolute spectrum of GRW + 70°5824 (Oke 1990) used for most of the WFPC2 calibration cuts off at 920 nm, short of the passband of several of the redder WFPC2 filters. To extend the spectrum to longer wavelengths, the spectrum of HZ43 (Bohlin *et al.* 1995), a white dwarf with similar spectral type, was scaled to match the Oke (1990) spectrum in the F791 filter. We then measured the stellar signal in the images (corrected for cosmic rays) using a range of photometric apertures from 5 to 25 pixels. The ratios of the observed to predicted counts in the 25-pixel aperture were similar for all filters *except* F1042M.

To bring the F1042M filter into accord with the other filters, we derived a multiplicative scale factor of 1.228 to apply to the nominal 1997 $\eta(\lambda)$ throughput for F1042M. This results in a 18.6% reduction in the derived I/F compared to the nominal HST calibration, eliminating the initially large discrepancy between our HST results and ground-based observations. This correction factor is probably uncertain by several percent, due in part to the uncertainty associated with the composite standard star spectrum over this wavelength range, and the uncertain extent of the broad scattered light halo of the F1042M filter. The typical uncertainty in the absolute photometry is on the order of a few percent, which reflects both uncertainties in the solar spectrum (particularly in the UV and

near IR) as well as in the absolute flux calibration for each filter.

2.3. Image Geometry and Ring Radius Scale

The PC has a 37″ × 37″ field, too small to contain the full ring system. Instead, to capture the entire planet and rings during each HST visit, we targeted the east and west ansae in separate sets of images. We placed the rings near the center of the field of view to minimize the effects of known optical distortions, which are most pronounced near the corners of the chip, and used the wavelength-dependent Trauger *et al.* (1996) polynomial mapping to convert between raw pixel coordinates and the standard WFPC2 distortion-corrected global coordinate system. The scale of each image (in km per pixel at Saturn) was computed from the angular extent of each PC pixel and the HST–Saturn separation at the time of each image. We found that the angular orientation of the image on the sky as recorded in the image header was extremely accurate, except in isolated instances where the STScI processing software inserted erroneous values for the first few images in a given visit. (These were easily identified, but readers who wish to reproduce the processing described here should be alert to these occasional errors).

The remaining factors needed to define an absolute coordinate system in the sky plane were corrections to the nominal pointing of each image, which was typically in error by about 1″ (20 PC pixels). Although some of the major satellites were occasionally in the field of view, their ephemerides are not sufficiently accurate to give sub-pixel accuracy in the ring plane radius scale (in a typical PC image, 1 pixel = 285 km in the sky plane at Saturn). Therefore, we used the rings themselves to determine the absolute pointing of each image. After some experimentation, we adopted the Encke Division within the A ring as the primary fiducial. (By choosing a symmetrical gap in the rings, rather than an outer or inner ring edge, we avoided having to compensate for the wavelength-dependent resolution in each image). We iteratively determined by least squares the global coordinates of the center of Saturn such that radial reflectivity scans across the Encke Division over a range of ring longitudes had their minima at the midpoint radius of the Encke Division of 133,584 km. This process converged quickly, and comparisons of radial scans shown below confirm that the derived radius scale for each image is accurate to about the 100-km (<0.3-pixel) level.

To allow for easy intercomparison of radial and azimuthal reflectivity scans, we reprojected the ring region of each image (after the 2D scattered light correction was obtained as described below) into a rectilinear grid (r, θ) as a function of ring plane radius r and ring longitude θ, measured in a prograde sense relative to the sub-Earth longitude (i.e., $\theta = 90°$ for the west ansa and $\theta = 270°$ for the east ansa). We preserved the observed flux in each pixel by rebinning each raw PC pixel in 20 × 20 sub-pixels and redistributing the signal into the appropriate cells in an (r, θ) grid with a resolution of 100 km in radius and 0.1°

in θ. Radial scans were taken by determining the median I/F at each radius over an azimuthal range of $\pm 5°$ centered on each ring ansa where the radial resolution is the highest. (For $B = -10°$ and $r = 100,000$ km, this corresponds to an azimuthal extent of $\simeq 10$ PC pixels). By taking the median rather than the average, we filter out cosmic ray hits in the images.

2.4. Corrections for Scattered Light

Thanks to the HST's corrective optics, the WFPC2 images are nearly diffraction limited for the bright cores of stellar images, but it is well known that there is a faint halo of scattered light that extends hundreds of pixels from a bright source such as Saturn's rings. In contrast-enhanced PC images, this scattered light is most easily seen outside of the bright A ring, inside of the C ring, and near the limb of the planet itself. In our initial radial I/F profiles, it shows up as a residual few percent signal in the free space regions adjacent to the rings. Light is being scattered out of the brightest ring regions into the fainter regions. Left uncorrected, the derived C ring and Cassini Division I/F's would be systematically too high, and the A and B ring reflectivities too low.

If the images had infinite SNR and we had perfect knowledge of the point spread function (PSF) for each filter, we could deconvolve each image, thereby correcting for the low level scattered light in the PSF halos. However, noise in the images and uncertainty in the PSF's conspire to doom this direct approach. Synthetic PSFs taking into account the detailed optics of the WFPC2 and HST can be generated using "Tiny Tim" (Krist and Hook 1999; `http://www.stsci.edu/software/tinytim/tinytim.html`), but this procedure cannot reproduce the observed scattered light at great distances from the source (Biretta 1996), as is well known by galactic observers (McLure *et al.* 2000).

Our present goal is to correct for regional systematic variations in ring brightness due to scattered light, rather than to retrieve the high-resolution ring structure that has been smoothed by the PSFs. We have developed a technique which avoids the introduction of high spatial frequency noise characteristic of direct deconvolution schemes, while at the same time taking account of the two-dimensional geometry of the rings, which are the ultimate source of the scattered light. We assume that the observed image $(I/F)_{\mathrm{obs}}$ can be represented approximately as a convolution of the ideal image $(I/F)_{\mathrm{ideal}}$ and a spatially invariant PSF:

$$(I/F)_{\mathrm{obs}} = (I/F)_{\mathrm{ideal}} \otimes \mathrm{PSF}. \qquad (2)$$

We would like to determine an approximation for $(I/F)_{\mathrm{ideal}}$ that corrects for low level scattered light; the difference between the two is simply

$$(I/F)_{\mathrm{obs}} - (I/F)_{\mathrm{ideal}} = (I/F)_{\mathrm{ideal}} \otimes \mathrm{PSF} - (I/F)_{\mathrm{ideal}}. \qquad (3)$$

As long as we care only about low spatial frequencies of the image, which are affected primarily by the faint wings of the PSF, the right-hand side (RHS) of Eq. (3) can be approximated

as the difference between the observed image, convolved with the PSF, and the unmodified observed image; that is,

$$(I/F)_{\mathrm{ideal}} \otimes \mathrm{PSF} - (I/F)_{\mathrm{ideal}} \simeq (I/F)_{\mathrm{obs}} \otimes \mathrm{PSF} - (I/F)_{\mathrm{obs}}. \qquad (4)$$

By combining these results, we obtain a "compensated" image $(I/F)_{\mathrm{comp}}$—an approximation to the ideal deconvolved image, corrected for scattered light:

$$(I/F)_{\mathrm{ideal}} \simeq (I/F)_{\mathrm{comp}}$$
$$= (I/F)_{\mathrm{obs}} - [(I/F)_{\mathrm{obs}} \otimes \mathrm{PSF} - (I/F)_{\mathrm{obs}}]. \qquad (5)$$

The square-bracketed term is positive in intrinsically faint regions into which light has been scattered from nearby bright regions and is negative in bright regions from which scattered light has been removed. Thus, the compensation scheme subtracts the extraneous light that has been scattered into the faint rings and free space regions of the image and restores it to its original source, the bright ring regions. This approximation is valid to the extent that the underlying low frequency structure of interest in the image is not greatly affected by the convolution. In our case, as long as the ideal image is not strongly altered by the first PSF convolution (i.e., by the optics of the system), then a second *digital* convolution will have approximately the same regional effect as the first. The first term in brackets on the RHS of Eq. (5) represents a smoothed version of the image. However, note that the first and third terms on the RHS combine to effectively double the amplitude of the high-resolution structure. To avoid this artifact, we smooth the 1D profile obtained from the "correction image" represented by the term in brackets on the RHS of Eq. (5), before we subtract it from the 1D profile obtained from the image represented by $(I/F)_{\mathrm{obs}}$. This preserves the nominal high-resolution structure of the original observed image while at the same time correcting for the broad "halo" of scattered light.

It is important to take into account the two-dimensional nature of the image when correcting for the large-scale systematic effects of low levels of scattered light. Figure 3 shows the rings at a moderate opening angle, characteristic of our observations. The concentric circles to the right, centered in the Cassini Division, have radii corresponding to encircled energies of 0.90, 0.95, and 0.98 for a Tiny Tim PSF for the F555W filter. Notice that scattered light from the bright A and B rings on several sides can contribute substantially to the measured signal in the Cassini Division. The effect is even more extreme for the actual PSFs. In the left-hand set of encircled energy contours, centered in the C ring, we have included a more realistic measure of the PSFs scattered light halo, taking them to have a power law angular dependence (as discussed below). The measured intensity in the C ring is contaminated by light scattered in from the adjacent B ring on three sides, and from the planet to some extent as well.

Figure 4 illustrates our implementation of the scattered light compensation scheme described above for a typical F555W image. In the top panel, the observed radial profile $(I/F)_{\mathrm{obs}}(r)$ is
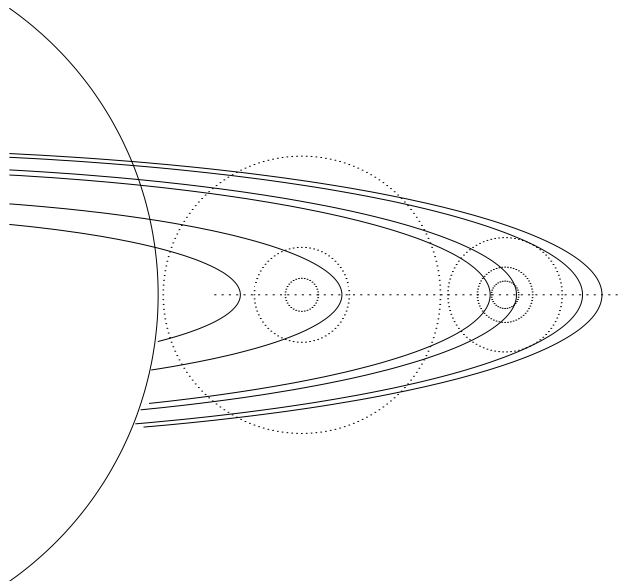
FIG. 3. Encircled energy contours for F555W PSFs, showing why a 2D convolution is needed to correct for PSF effects. The circles correspond to fractional encircled energies of 0.90, 0.95, and 0.98. The standard Tiny Tim PSF is shown at the right, while a more realistic PSF with a power law halo of slope $k = -2.5$ is shown at the left. See Section 2.4 for discussion.

the residual scattered light has been removed by this process. We have found that, in general, Tiny Tim cannot properly model the extended PSF halos known to be present (except for the F1042M filter); thus, we adopted a composite model consisting of a PSF core as given by Tiny Tim, along with a radially symmetric skirt that followed a power law of constant index, grafted onto the original PSF at a radius of 4 pixels. Using this approach, we could nicely match the representative scattered light halo shown in Biretta (1996; their Fig. 5.9) for the F555W filter, using a power law slope of $k = -2.5$ (Fig. 5). We varied the slope of the power law halo in steps of 0.05 and adopted as our final PSF for each filter that which most nearly eliminated the scattered signal in the free space regions adjacent to the rings. The adopted power law indices are included in Table II. For most filters, k
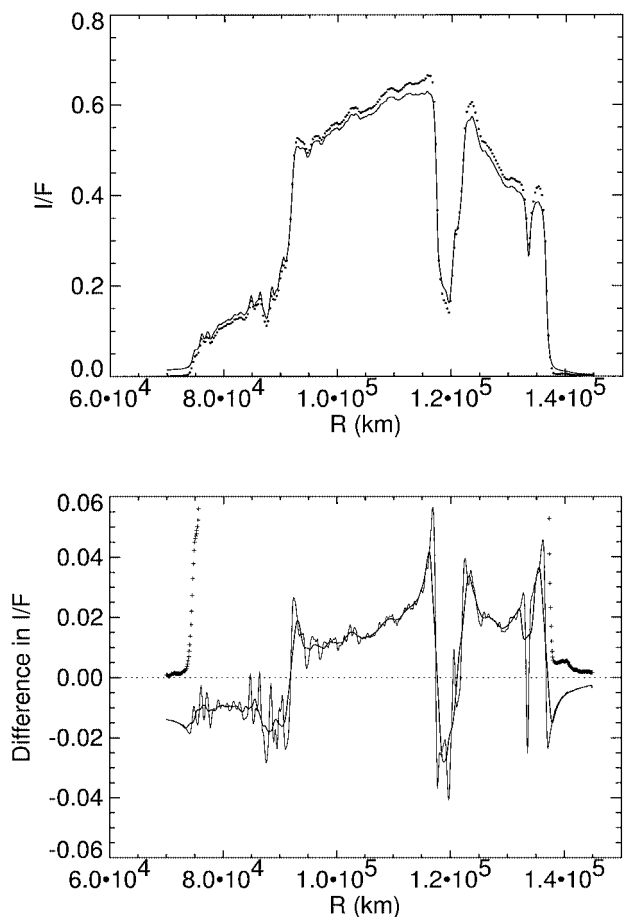
shown by a smooth curve. Notice the substantial residual signal interior to the C ring ($r < 75,000$ km) and exterior to the A ring ($r > 137,000$ km). We convolved the original pipeline-processed two-dimensional image with an adopted PSF and determined the radial reflectivity profile $[(I/F)_{obs} \otimes PSF](r)$ of the resultant image in exactly the same fashion as for the original image. We then formed the difference between these two radial profiles, shown as the solid lines in the bottom panel of Fig. 4. Notice that the difference is substantial (a few percent), varying from strongly negative in the C ring and Cassini Division, to positive in the A and B rings. To avoid doubling the amplitude of the high-resolution structure when adding this correction term to the original radial profile, we boxcar smoothed the correction signal with a 2100-km-wide filter, resulting in the smooth bold solid line in the bottom panel. Finally, we added this smoothed correction function to the original radial scan, obtaining the compensated radial profile shown as plus symbols in the upper panel. The high-resolution features of the original (solid line) profile are preserved, while the light that had been scattered out of the bright A and B rings has been restored and the extraneous light scattered into the C ring and Cassini Division has been removed.

One measure of the effectiveness of the compensation procedure is the level of residual light in the free space regions adjacent to the rings. The curve with + symbols in the bottom panel of Fig. 4 shows the compensated radial scan at an expanded vertical scale. Comparison of the + profile with the correction profiles (light and heavy solid curves in bottom panel) and with the original scan (solid curve in upper panel) shows that most of

FIG. 4. Comparison of original and compensated radial ring reflectivity profiles for one image in the F555W filter. In the upper panel, the original radial profile is shown by the smooth curve and the compensated profile is shown by the + symbols. After compensation, the residual flux in the free space regions adjacent to the rings is greatly reduced, and the light scattered away from the bright A and B rings has been restored. The bottom panel shows the unsmoothed and smoothed correction functions to be applied to the original I/F scan, and the + symbols again show the corrected curve from the upper panel, at an expanded radial scale. There is little or no residual free space scattered signal after the compensation process has been applied (compare solid and + curves in upper panel, also).
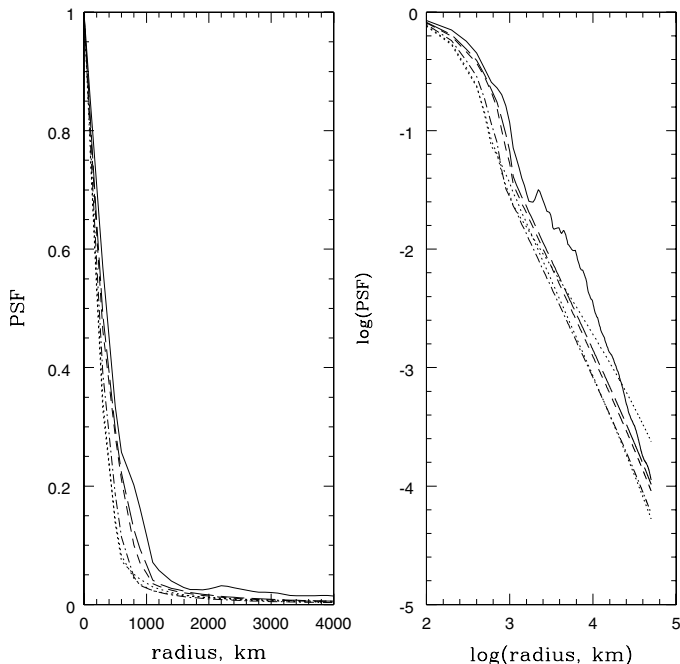
FIG. 5. One-dimensional integrals of adopted WFPC2 PSFs, all having power law halos (as described in Section 2.4) except for F1042M. Curves are: F255W and F336W (dotted, F255W with broad halo visible in right-hand panel), F555W (dot–dash), F814W (short dash), F785LP (long dash), and F1042M (solid).

was close to -2.5, although we found that the F255W filter had a substantial scattered light halo that required a rather flat spatial index of $k = -2.10$. Since version 5.0a of Tiny Tim includes what is claimed to be an accurate calculation of the F1042M PSF halo, we used this PSF without further modification.

We tested the robustness of this scheme on synthetic images with intrinsically sharp-edged rings which we then convolved with a known PSF. We applied the compensation method to this artificial observation and recovered the original sharp-edged ring structure and original I/F levels to very high accuracy. The main source of error lies in the approximation of the PSF as a composite of a sharp core with an axisymmetric halo. The true scattered signal is known to be spatially variable and streaky and cannot be modeled from simple assumptions. Nevertheless, we estimate that the compensation technique accurately corrects for regional scattered light variation at the 1–2% level, comparable to the uncertainty in the conversion factors between I/F and raw DN.

Although the radial scan bins are uniformly spaced at 100 km, the actual radial resolution is, of course, limited by the resolution of the HST. As we have seen, for the nearly diffraction-limited PC images, the PSF is wavelength dependent, and since we are looking for regional variations in ring reflectivity as a function of wavelength, it is important not to misidentify wavelength-dependent resolution as evidence for color variations in regions where I/F changes rapidly with radius. We have integrated our adopted PSFs into one-dimensional versions to simulate the

averaging effect of the PSF on the high-resolution structure of our derived radial profiles (Fig. 5). We use these below to smooth the compensated I/F profiles to a common radial resolution.

3. RESULTS

3.1. Radial Reflectivity Profiles at Different Wavelengths

Typical radial I/F scans of our images, compensated for scattered light as described above, are shown by the heavy curves in Figs. 6 and 7. Figure 6 shows the entire ring profile in several different HST passbands, and Fig. 7 shows enlarged versions which allow the potential effects of wavelength-dependent PSFs to be seen more clearly. In Figs. 6 and 7, boundaries are indicated for regions over which average colors and spectra have been obtained. These regions (see Table IV) are refinements of those suggested on the basis of Voyager color data (Estrada and Cuzzi 1996) and structural scales (Horn and Cuzzi 1996), based on results presented here and by Cuzzi *et al.* (2000). In this paper we do not refer to or analyze regions where differential resolution artifacts are suspected, but the nomenclature allows these regions to be added in the future. The reflectivity profiles are qualitatively compatible with the Voyager scans obtained by Estrada and Cuzzi (1996), as seen by comparison with Voyager profiles which have been smoothed by the appropriate HST PSFs (shown as thin lines in Figs. 6 and 7). Close inspection reveals small regional differences between the two sets of scans, which might be caused by illumination and viewing differences. Smoothing a 1D Voyager radial profile by a 1D version of our HST PSFs is only an approximation of the 2D HST smoothing effect, and agreement between 1D-convolved profiles does not necessarily indicate regions to be free of PSF effects. For instance, the central part of the Cassini Division seems to be free of PSF effects (except at F1042M) from inspection of the smoothed Voyager data. However, our actual 2D convolutions (Section 2.4) indicate that the Cassini Division is in fact contaminated by light from the surrounding rings at *all* wavelengths, which is corrected out to first order by the technique discussed in Section 2.4. Nonetheless, the PSF-smoothed Voyager profiles do provide a sense of consistency between the HST and Voyager data.

It is of interest to note that the ring I/F is only weakly correlated with the underlying optical depth (cf. Dones *et al.* 1993). First, the I/F increases monotonically outward, while the optical depth reaches a maximum in the mid B ring. Furthermore, close inspection reveals that the local reflectivity maxima in the mid B ring do not align with the optical depth maxima. We return to correlations of this type in Section 3.3.

3.2. Phase and Opening Angle Dependence of Ring Reflectivity

Direct comparison of reflectivity profiles across varying geometries is complicated by the fact that the ring reflectivity variations with illumination and viewing geometry depend on
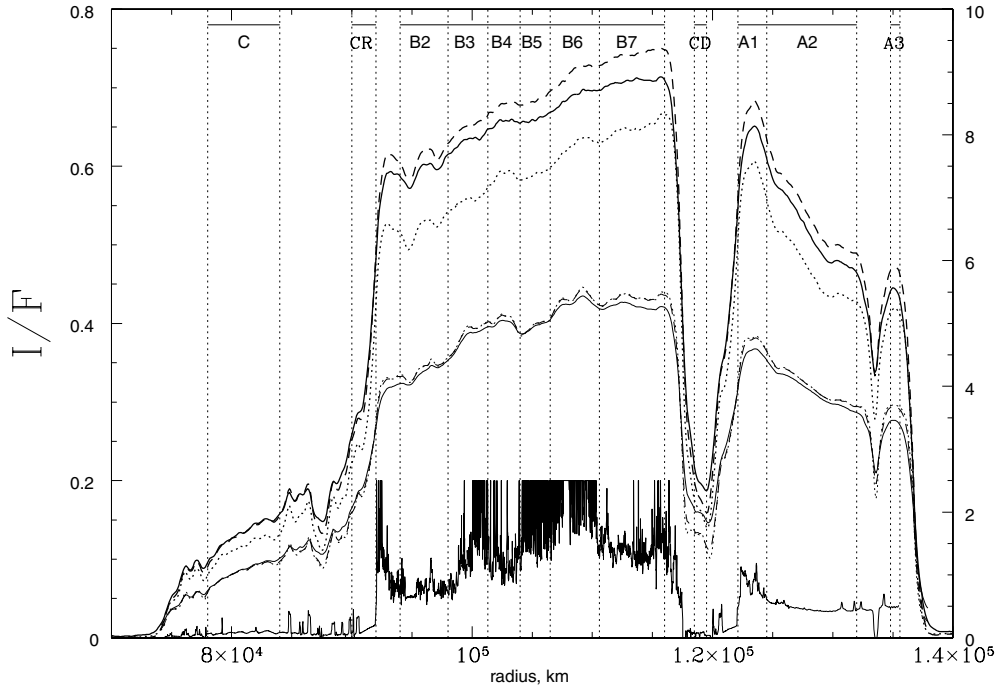
FIG. 6. Typical HST scans (heavy curves) at several wavelengths. The HST filter bands shown are, in order of increasing effective wavelength, F555W (dotted), F814M (short dash), and F1042M (solid). The opening angle is $B = -10°$ and the phase angle is $\alpha = 0.5°$ for these observations. Different convolutions of the Voyager 2 G filter radial reflectivity profile are shown in the lightcurves at lower amplitude, obtained at a different geometry; the PSFs used to smooth the Voyager profiles corresponded to the HST passbands shown. These profiles provide a measure of the role of wavelength-dependent resolution in ratios of the HST data. Also shown (lower solid curve) is the Voyager ISS normal optical depth profile obtained by the first author (see Dones *et al.* 1993 and Nicholson *et al.* 2000), plotted against the right-hand scale. This data set, while incomplete in the outer A ring, more accurately represents the distribution of high optical depth material in the B ring than the more familiar Voyager PPS data set. Regional boundaries are given in Table IV.

optical depth, and the optical depth varies with location. For the geometry of the Voyager observations, ring reflectivity is dominated by single scattering (Cuzzi *et al.* 1984, Dones *et al.* 1993). In this regime, those factors entering into the reflectivity which depend on the optical depth and geometry cancel out of ratios taken of the reflectivity at a given time and geometry, but at different wavelengths (Cuzzi and Estrada 1998). Although the ring vertical structure is believed to deviate from that of a classical many-particle-thick layer (Dones *et al.* 1989, 1993; Salo 1992, 1995; Richardson 1994), the standard classical expression for reflected reflectivity at wavelength λ in the single scattering limit (Chandrasekhar 1960; see also Cuzzi *et al.* 1984) remains conceptually useful:

$$\frac{I}{F} = A_\lambda P_\lambda(\alpha) \frac{\mu_0}{4(\mu + \mu_0)} \left[1 - \exp\left(\frac{-\tau(\mu + \mu_0)}{\mu\mu_0} \right) \right]$$
$$\equiv A_\lambda P_\lambda(\alpha) O(\tau, \mu_0, \mu). \tag{6}$$

Both the reflected intensity I and the incident flux πF are functions of λ, but their λ-dependence will remain implicit following traditional usage. A_λ is the ring particle single-scattering albedo, $P_\lambda(\alpha)$ is the ring particle phase function as a function of phase angle α, $\mu_0 = \sin|B'|$ is the cosine of the incidence

angle (sine of the solar elevation angle), τ is the normal optical depth, and $\mu = \sin|B|$ is the cosine of the emission angle (sine of the Earth elevation angle). In the actual rings, the scattering function $O(\tau, \mu_0, \mu)$ might be different from the classical expression (Dones *et al.* 1989) but it will still be separable from the product $A_\lambda P_\lambda(\alpha)$ if single scattering dominates.

The dependence of I/F on (μ_0, μ) through the function $O(\tau, \mu_0, \mu)$ varies with radially varying τ. Thus, because μ and μ_0 are different for each observation, there is no single multiplicative factor by which we can simply scale a particular I/F profile and expect good agreement with another I/F profile obtained in a different illumination and/or viewing geometry. For instance, as shown in Fig. 8a, the reflectivity of the regions with lower optical depth (C ring and Cassini Division) is larger at the lower ring elevation angles of the Voyager data, *relative* to the reflectivity of regions with higher optical depth (A and B rings). The reflectivity profiles do not vary monotonically with opening angle.

The approximate validity of the "classical" $O(\tau, \mu_0, \mu)$ given in Eq. (6) may be assessed by applying it as a radially variable, optical-depth-dependent correction factor to scale ring I/F values from one geometry to another. To accomplish this, we averaged the Voyager PPS optical depth profile to the binning of our I/F scans and scaled several I/F profiles to a common
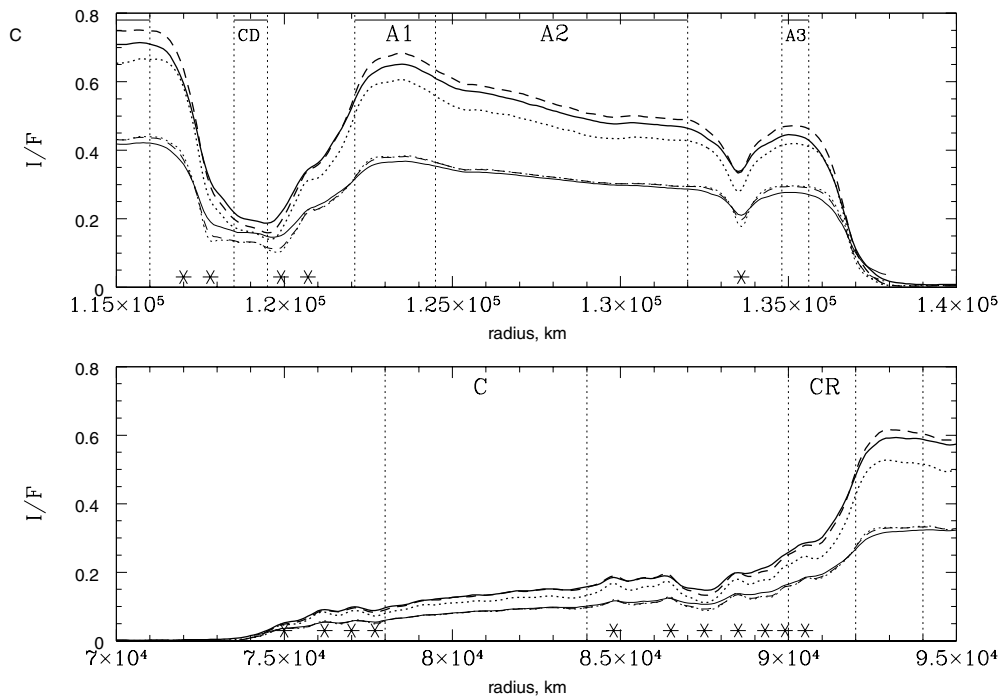
FIG. 7. Expanded versions of Fig. 6, designed to indicate trouble areas where differential resolution between the HST PSFs might introduce artifacts. The HST filter bands shown are, in order of increasing effective wavelength, F555W (dotted), F814M (short dash), and F1042M (solid). As in Fig. 6, radial regions are indicated where Estrada and Cuzzi (1996) and Horn and Cuzzi (1996) suggested that ring properties seemed to change (values in Table IV). In the PSF-smoothed versions of the *same* Voyager high-resolution profile (light curves), note how certain abrupt features show wavelength-dependent differences in structure due *only* to the PSF variations. Such regions (denoted by asterisks) will produce color ratios which are artifacts. Note in the Cassini Division how significantly the F1042M reflectivity is increased by PSF effects, relative to other wavelengths. Even after correction by the functions described in Section 2 and Fig. 4, the heavy curves above show some hint that the PSF effect has not been completely removed from the F1042M data (see Section 3.3.4).

geometry using the ratio of the appropriate $O(\tau, \mu_0, \mu)$ functions as in Eq. (6). The results are shown in Fig. 8. One part of the correction, which is essentially all that affects the A and B rings, is the purely geometrical fraction $\mu_0/(\mu + \mu_0)$, which differs from 0.5 in both directions at the tens of percent level since μ and μ_0 are roughly but not exactly equal in Earth-based geometries. The other part is the τ-dependent exponential term, which makes the optically thin rings fainter as the opening angle increases. The fact that both terms come into play may be seen by study of Fig. 8.

The good agreement between the corrected curves in the C ring and Cassini Division in Figs. 8b and 8c indicates that classical, single-scattering behavior describes these regions fairly well over this range of elevation angles. Naturally, the good agreement in the C and A rings would not be found if τ itself were dependent on λ over this spectral range. Note that the inner B ring behaves like a classical layer except for at the very lowest opening angles. Also notice that the mid A ring has a weak trend in the opposite direction from the optically thick B ring regions. If this is real, it may be due to an opening-angle dependence of the A ring's well-known quadrupole brightness asymmetry (Dones *et al.* 1993, French *et al.* 2000).

However, the corrected profiles diverge significantly in the optically thicker regions (middle and outer B ring, optically thickest parts of the A ring). A study of Fig. 8a reveals that the optically thick rings get brighter as the rings open up—rather than either remaining the same or getting marginally fainter as would a classical, single scattering layer with $\mu = \mu_0$. This might be explained either if multiple interparticle scattering played an increasing role in these divergent regions as the ring opening angle increases or if the classical (many particle thick) layer scattering function underestimates the opening angle dependence of the scattering function. Note also that the relative magnitude of the divergence is very similar between the F555W and F336W data (Figs. 8b and 8c), even though the particles are only half as bright at 336-nm wavelength. This indicates that multiple interparticle scattering is not responsible for the outer B ring (optically thick region) divergences. In Section 3.3 below, we will show further evidence that multiple interparticle scattering is *not* playing an increasing role as the opening angle increases. These independent but mutually supportive results argue for regional variations in the vertical structure of the rings, relative to a "classical" layer, with the optically thickest regions of the B ring behaving the least like a classical model. We return to this in Section 4.2.

TABLE III
WFPC2 Observations of Saturn's Rings

Figures	α (°)	B (°)	B' (°)	Filters
6, 7	0.49	−10.12	−10.22	F555W, F814W, F1042M
8	5.67	−3.72	−6.24	F336W, F555W
	6.02	−8.88	−11.47	F336W, F555W
	6.26	−16.67	−14.38	F336W, F555W
	6.10	−21.04	−19.36	F336W, F555W
	6.10	−24.19	−22.92	F336W, F555W
9	6.02	−8.88	−11.47	F439W
10	2.00	−10.59	−10.01	F336W, F555W
	0.98	−10.28	−10.15	F336W, F555W
	0.50	−10.12	−10.22	F336W, F555W
	0.30	−9.99	−10.28	F336W, F555W
	6.02	−8.88	−11.47	F336W, F555W
11, 12	0.46	−4.31	−4.73	F336W, F555W
	1.92	−3.82	−4.93	F336W, F555W
	5.67	−3.72	−6.24	F336W, F555W
	2.00	−10.59	−10.01	F336W, F555W
	0.98	−10.28	−10.15	F336W, F555W
	0.50	−10.12	−10.22	F336W, F555W
	0.30	−9.99	−10.28	F336W, F555W
	6.02	−8.88	−11.47	F336W, F555W
	6.26	−16.67	−14.38	F336W, F555W
	0.69	−15.43	−15.47	F336W, F555W
	0.32	−15.25	−15.56	F336W, F555W
13	2.00	−10.59	−10.01	F255W, F555W
	0.30	−9.99	−10.28	F255W, F555W
	6.26	−16.67	−14.38	F255W, F555W
	0.69	−15.43	−15.48	F255W, F555W
14	2.00	−10.59	−10.01	F255W, F336W
	0.30	−9.99	−10.28	F255W, F336W
	6.26	−16.67	−14.38	F255W, F336W
	0.69	−15.43	−15.48	F255W, F336W
	1.99	−23.33	−23.96	F255W, F336W
15b	0.98	−10.28	−10.15	F785LP, F814W
	0.32	−15.24	−15.56	F785LP, F814W
	0.30	−19.90	−20.20	F785LP, F814W
	1.99	−23.33	−23.96	F785LP, F814W
16	0.49	−10.12	−10.22	F814W, F1042M
	6.02	−8.88	−11.47	F814W, F1042M
	1.20	−15.57	−15.42	F814W, F1042M
	6.10	−21.04	−19.36	F814W, F1042M
	0.42	−19.98	−20.16	F814W, F1042M
17	0.98	−10.28	−10.15	F785LP, F814W
	6.26	−16.67	−14.38	F225W, F336W, F439W, F555W, F675W, F814W
	1.20	−15.57	−15.42	F814W, F1042M
	0.69	−15.43	−15.48	F225W, F336W, F439W, F555W, F675W, F814W

3.3. Color Ratio Profiles: Motivation and Sources of Uncertainty

The difficulties of comparing reflectivity (I/F) profiles across a range of observing geometries, as discussed above, motivate finding other ways to explore ring particle properties. Cuzzi and Estrada (1998) argued that, since single scattering dominated

in the Voyager geometry, the terms $A_\lambda P_\lambda(\alpha)$ and $O(\tau, \mu, \mu_0)$ (Eq. (6)) were separable. Furthermore, since the ring optical depth (dominated by large particles) is wavelength independent, $O(\tau, \mu, \mu_0)$, containing all the optical depth and geometric information, cancels out of ratios taken between wavelengths at the same time and geometry, leaving only ratios of $A_\lambda P_\lambda(\alpha)$. However, we will show below that one key premise of Cuzzi and Estrada (1998) was invalid. They argued, based partly on icy satellite data, that the phase functions $P_\lambda(\alpha)$ of macroscopic icy bodies would be nearly wavelength independent, and thus the I/F ratios would be essentially ratios of A_λ. It turns out, instead, that $P_\lambda(\alpha)$ does vary significantly with λ. Subsequent sections will emphasize ratios of ring reflectivity observed by HST at different wavelengths, interpreting them as radial profiles of the function $A_\lambda P_\lambda(\alpha)$.

Sources of uncertainty in HST data. In all cases, ratios are constructed from ring scans in different filters, obtained on the *same* ring ansa during the *same* HST orbit, to minimize the chance for "noise" to be introduced by misregistration due to residual distortion and/or navigation errors. An example of the expected noise level due to misregistration is shown in Fig. 9, in which scans obtained from four different images taken with the F439W filter on the same ansa, on the same orbit, are made into three ratios. Over most of the rings, the peak-to-peak noise amplitude in the ratio scans is at about the 10% level.

Taking ratios of scans obtained from images at *different* wavelengths introduces a small amount of additional noise at sharp edges, because of the differences between the PSF's at the various wavelengths (Fig. 5). We have conducted simulations to estimate the uncertainties due to this effect by smoothing a single Voyager G filter scan with several different HST PSF's. Differences can be seen directly in the unlabeled radial sections of the radial profiles, near narrow bands in the C ring, the edges of the Cassini Division region, the Encke gap, and the outer A ring (Fig. 7), and artifacts appear in the ratios of these scans (denoted by asterisks in subsequent figures discussed in Section 3). These simulations indicate that valid color ratio information can

TABLE IV
Radial Boundaries of Ring Regions

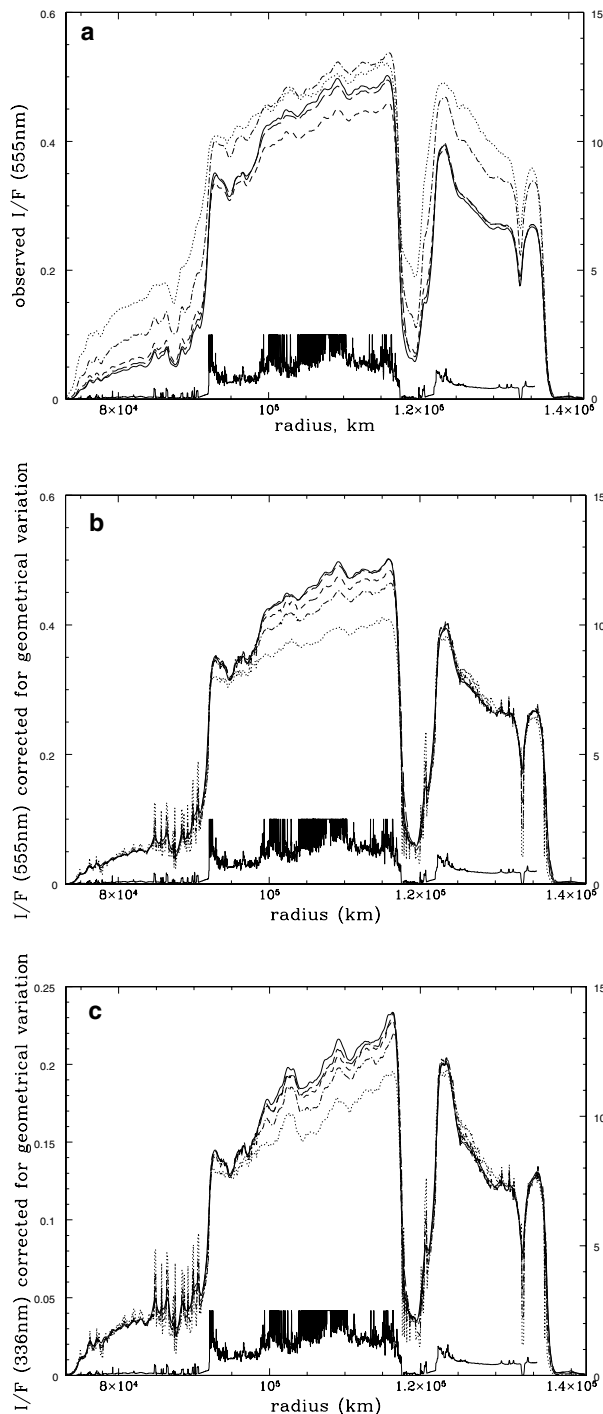| Ring region	Inner (km)	Outer (km)
C	78,000	84,000
CR	90,000	92,000
B2	94,000	98,000
B3	98,000	101,300
B4	101,300	104,000
B5	104,000	106,500
B6	106,500	110,600
B7	110,600	116,000
CD	118,500	119,500
A1	122,100	124,500
A2	124,500	132,000
A3	135,600	134,800

FIG. 8. Agreement or deviation between ring scattering and classical single-scattering behavior, as a function of ring radius at five different ring opening angles. (a) Top panel: profiles were obtained from F555W data at phase angle of $\alpha = 6°$, and ring opening angles $B = -4°$ (dotted), $-10°$ (dot-dashed), $-15°$ (short dash), $-20°$ (long dash), and $-24°$ (solid). The Voyager ISS optical depth profile is shown in the lower solid curves (right scale). (b) Middle panel: The F555W I/F profiles were all scaled to the $B = -24°$ geometry using the appropriate factors for their local optical depth as given by the function $O(\tau, \mu_0, \mu)$ in Eq. (6). (c) Lower panel: The same procedure was followed for profiles obtained in the F336w filter at the same set of geometries. For further discussion see Sections 3.2 and 4.2.
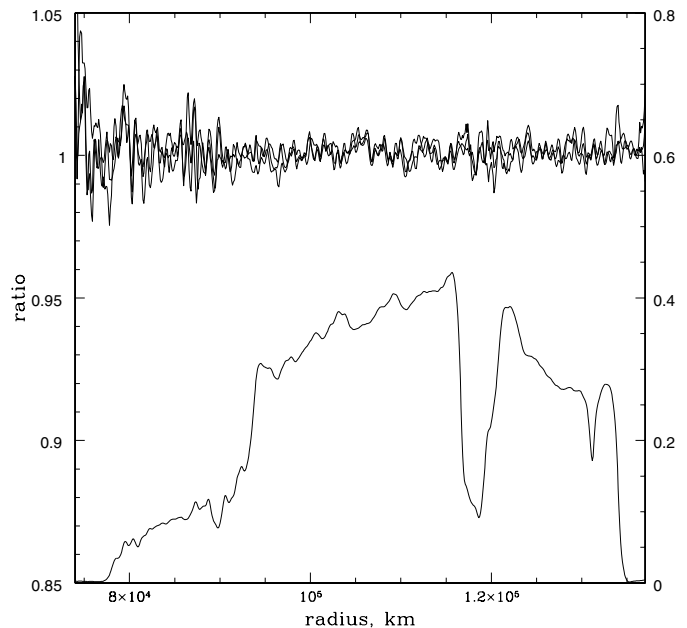
FIG. 9. Typical noise expected from the ratio technique, as illustrated by ratios between four F439W scans taken on the same ansa and visit. Also shown is one such F439W I/F scan (right scale). Note that, for the same wavelength and geometry, even the abrupt A and B ring edges remain free of ratioing artifacts at the 1% level. There is increased noise associated with relatively narrow features in the C ring, partly because of the lower reflectivity levels there.

still be obtained even in the center of the Cassini Division and in the band between the Encke gap and the outer edge of the A ring (see Fig. 7). Overall, while caution is appropriate in interpreting the smallest wiggles in the curves, features at the 2–3% level, away from sharp edges, seem to be believable. Furthermore, many features reappear in independent scans obtained in different geometries.

Sources of uncertainty in Voyager data. The primary source of error in the Voyager data is in the absolute calibration as a function of wavelength. It is known that the camera sensitivities changed since their initial calibration by Danielson *et al.* (1981); however, there has been a long-running debate in Voyager imaging circles as to just what the correct calibration is, especially in the UV. The alternate atmospheric- and satellite-based calibrations for the UV filter differ by 15% (Estrada and Cuzzi 1996), and typically their average is merely adopted as the Johnson–Buratti calibration (see Estrada and Cuzzi (1996) for a discussion).

On top of these basic calibration uncertainties, there was an error in the Voyager data reduction in (Estrada and Cuzzi 1996, Estrada *et al.* in preparation). Essentially, the data reduction process of Estrada and Cuzzi (1996) incorrectly employed the older Danielson calibration rather than the newer Johnson–Buratti calibration as it had intended to do. All Voyager data in this paper, and in Estrada *et al.* (in preparation), are corrected to the "atmospheric" color calibration, as originally intended by Estrada and Cuzzi (1996).

3.3.1. Phase and Opening Angle Variation of Ring Color Ratios

To simplify comparisons between profiles taken in different geometries and at different wavelengths, we took ratios of profiles obtained in *the same* geometry, but in different filters. The qualitative agreement between the color ratio profiles (Figs. 10 and 11) is somewhat better than that between the reflectivity profiles themselves (Figs. 7 and 8).

Comparing these color ratio profiles obtained at different phase angles clearly reveals a substantial reddening with increasing phase angle in the 336–555-nm spectral range. This effect was not revealed by earlier observations of the rings, to our knowledge. For example, Fig. 10, showing F555W/F336W ratio profiles for five phase angles at a single opening angle of $B = -10°$, indicates that the F555W/F336W "redness" of the A and B rings increases by approximately 27% between 0.3° and 6.0° phase angles.

Furthermore, it seems fairly clear that the opening angle has a negligible effect on ring color—certainly compared to the substantial phase angle effect. This conclusion is illustrated in Fig. 11, which shows color ratio profiles in 12 geometries—three phase angles at each of four opening angles. Each profile is an average of east and west ansa ratio profiles. In fact, Fig. 11 makes it abundantly clear that the complex, regionally variable differences seen in Figs. 8b and 8c (in the B ring as the ring opening angle increases) can be explained simply by differences in the single scattering behavior—specifically, color—of the individual ring particles. That is, there is no dependence on opening angle of the F555W/F336W ratio. This is discussed more in Section 4.3.

In Fig. 12 we average all the profiles of Fig. 11 over ring opening angle, which decreases the noise and reveals considerable similarity between the radial shapes of the HST profiles at different phase angles, while the overall redness increases. We also show a smoothed Voyager profile, for comparison. As mentioned above, the Voyager color profile incorporates a corrected calibration which reduces the G/UV ratio significantly from that in Estrada and Cuzzi (1996). Taken at face value, even the "atmospheric" calibration leaves the Voyager color ratio profile close to or even slightly *below* the HST profiles in the Cassini Division and inner B ring. Any of the other standard Voyager UV calibration schemes would make the rings even less red. If a more accurate Voyager calibration allowed the G/UV ratio to increase by 2–3% from the atmospheric values, the phase reddening would flatten in the C and inner B rings, but the Voyager profile would still be redder than the HST profile in the A ring. For display purposes, the Voyager ratio profile as plotted here has been biased upward by 5% from the nominal "atmospheric" calibration results to better allow comparison of features. Given the calibration uncertainty in the Voyager filter set, it seems that one cannot use the Voyager data to draw quantitative conclusions about phase-dependent reddening between 6° and 14°. However, the qualitative agreement between the shape of the (smoothed) Voyager and HST color ratio profiles is excellent, lending further
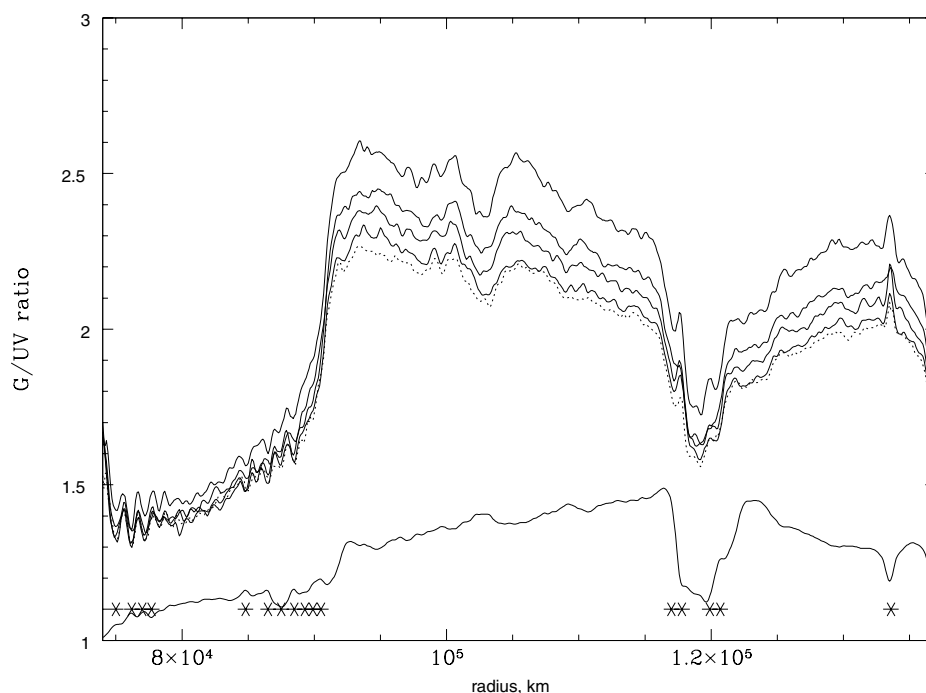

FIG. 10. HST F555W/F336W color ratios at five phase angles ($\alpha = 0.3°$, 0.5°, 1.0°, 2.0°, and 6.0°) at opening angle $B = -10°$. Each ratio profile is an average of east and west ansa profiles in the same geometry. The ring color gets redder with increasing phase angle, although there seems to be little variation between $\alpha = 0.3°$ (dotted curve) and $\alpha = 0.5°$ (solid curve, as are all other phase angles). Locations of probable artifacts in the HST ratios, produced near sharp edges by wavelength-dependent PSFs, are indicated by asterisks below the scans. Also shown (lower profile) is a radial profile of the ring I/F in the F336W filter.
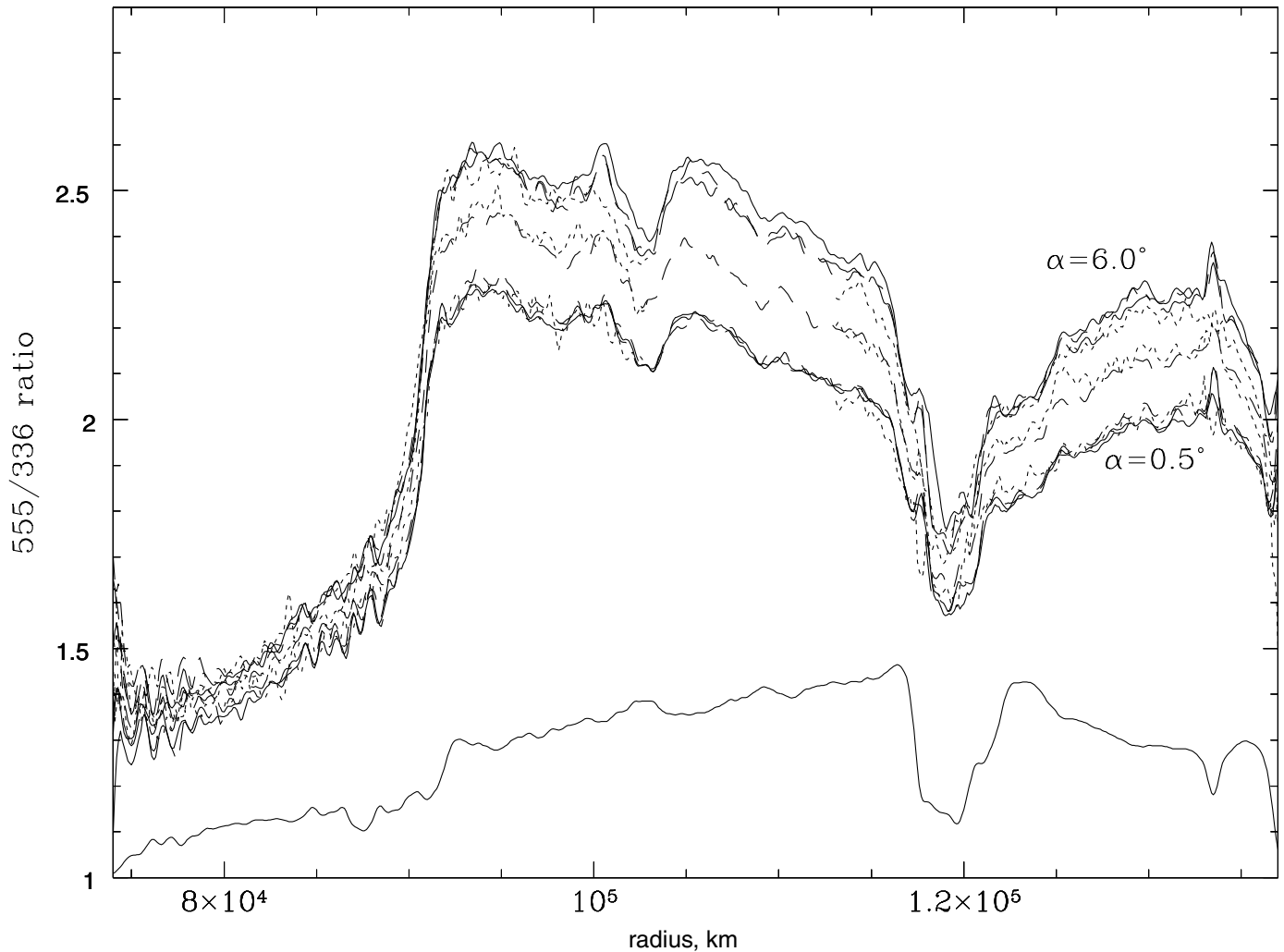
FIG. 11.   HST color ratios at three phase angles ($\alpha = 0.5°$, $2.0°$, and $6.0°$) and four elevation angles $B = -4°$ (dotted), $-10°$, (short dash), $-15°$ (long dash), and $-20°$ (solid). Most curves are averages of east and west ansa ratio profiles, where contamination by visually obvious spokes occurs in the B ring (only in dotted curves at $4°$ tilt) the curves are not plotted. Also shown is a F336W radial scan of the ring reflectivity at the same radial scale. There are clear systematic phase angle variations of color, as seen in Fig. 10, but there are no systematic variations with elevation angle. The lack of elevation angle dependence is most evident in the A and inner B rings. A small amount of opening angle dependence might be coming into play in the outer B ring, at a combination of the largest opening and phase angles (solid curve at $6.0°$ phase), where no spoke contamination is seen.

credibility to features seen in the HST reduction. Furthermore, ratioing Voyager NAC images against nearly simultaneous WAC images (Estrada *et al.*, in preparation) verifies the overall radial G/UV ratio profile, so the apparently larger phase reddening between $6°$ and $14°$ for the A ring *relative to* the inner rings mentioned above may still be correct.

We note that, in contrast to the *lack of* correlation between underlying optical depth and ring reflectivity in the B ring, Fig. 12 shows a fairly good positive correlation between underlying optical depth and ring *color*, on local scales (few 10^3 km). Regions with the highest optical depth do seem to align with regions having the largest 555/336 and G/UV color ratio (for example, around 100,000 and 106,000 km). The double-peaked feature near 100,000 km was more striking in full-resolution Voyager data and referred to by Estrada and Cuzzi (1996) as the "red

bands." On top of these local variations are larger scale color variations which do *not* correlate with optical depth (inward reddening in B ring).

3.3.2. Far UV: F555W/F255W and F336W/F255W Ratio Profiles

The F255W filter covers a spectral range never before studied at any meaningful spatial resolution. OAO observations have shown that overall, the ring spectrum flattens shortward of 300 nm, in contrast to the spectrum of the Galilean satellites which continue to darken toward shorter wavelengths (Caldwell 1975). Wagener and Caldwell (1986, 1988) confirm this with IUE spectra and also observe the 170-nm water ice absorption edge.
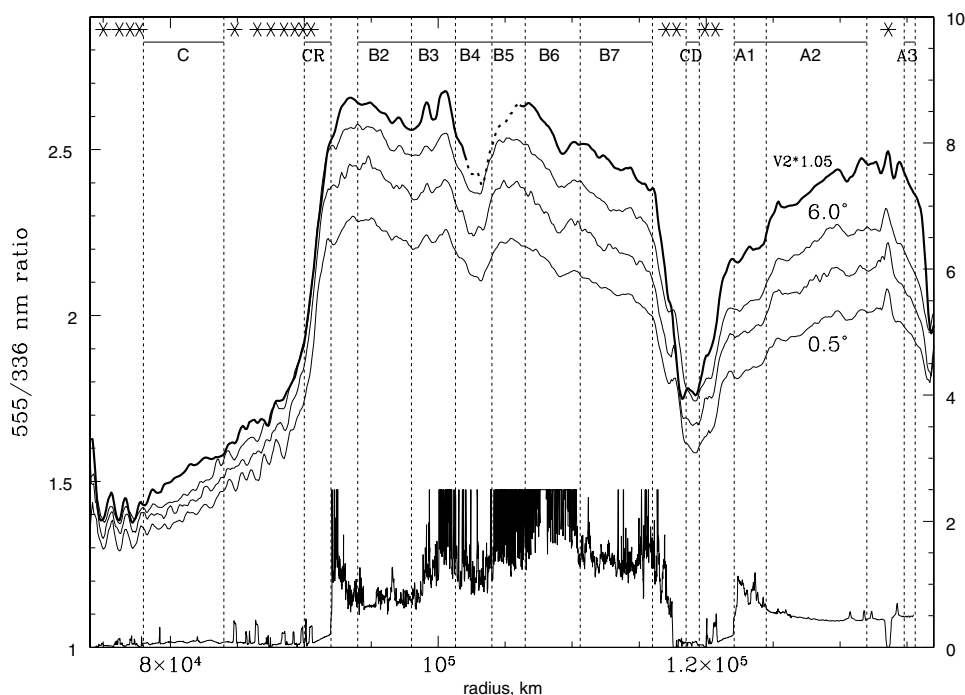
FIG. 12. Comparison of opening-angle-averaged HST color ratio scans with Voyager color and optical depth profiles. The Voyager color ratio profile (heavy line) is obtained by smoothing the Voyager G and UV I/F scans with the F555W and F336W HST PSF's, respectively, and ratioing the smoothed profiles. The ratio profile obtained this way (scaled up by 1.05 to separate it from the HST profiles) exhibits most of the same features, and artifacts at sharp edges, seen in the HST ratio profiles (artifacts indicated by asterisks). The dashed region in the Voyager profile is contaminated by a spoke, which is more prominently dark in the G filter than the UV filter (the HST averages do not include spoke-contaminated regions). The radial optical depth profile at the bottom (right scale) is obtained from Voyager ISS data by JNC (for a discussion see Dones *et al.* 1993 or Nicholson *et al.* 2000). It saturates at $\tau \approx 2.5$ due to loss of signal. Note the apparent correlation between the optically thickest regions and the local maxima in the 555/336 and G/UV ratios.

The radial profile of F555W/F255W color ratios is shown in Fig. 13. Based on the lack of opening angle variations in the more well-sampled F555W/F336W color ratios, we present the F555W/F255W ratios as a group even though they are split between opening angles of $B = -10°$ (phase angle $\alpha = 0.3°, 2.0°$) and $B = -15°$ ($\alpha = 0.7°, 6.3°$). The F555W/F255W ratio profile is superficially similar to the F555W/F336W profiles of Fig. 12 and also shows a prominent phase reddening—70% of the amount seen between the more widely spaced 336 and 555 nm filters, which supports the idea of a significant albedo gradient between 255 and 336 nm.

The F555W/F255W color ratio also shows structure in the middle B ring, which correlates with the relatively red region between 104,000 and 109,000 km and the local optical depth minimum just inside it; there is less evidence for any reddish bands around 100,000 km, as seen in 555/336 and apparently associated with the local optical depth maxima at 98,500–102,000 km. The difference between the F555W/F336W and F555W/F255W ratio profiles is most easily seen by directly taking the F336W/F255W ratio profile, which also minimizes differential resolution effects (Fig. 14). There are substantial radial variations even between these two closely spaced UV wavelengths. As with the F555W/F336W and F555W/F255W ratios and the Voyager ratios (Estrada and Cuzzi 1996), the color boundary between the B and C rings is not as sharp as the optical

depth boundary, plausibly related to ring evolution subsequent to meteoritic bombardment and ballistic transport (Cuzzi and Estrada 1998).

Notice especially the qualitative shape differences between the F336W/F255W profile and the F555W/F336W profile in the inner C ring and the A ring. The F336W/F255W ratio is not simply a scaled version of the F555W/F336W ratio. This suggests to us that a different material, with a different radial distribution, is responsible for the FUV absorption from whatever material produces the overall ring redness.

In another interesting distinction between the F336W/F255W ratio and those ratios involving the F555W reflectivity, the profile obtained by averaging over all four phase angles shows no convincing evidence for intermediate scale color variations, which correlate with underlying optical depth, such as are seen in the middle B ring in both Voyager G/UV and HST F555W/F336W ratio plots *and* the HST F555W/F255W ratio profile.

3.3.3. 850-nm Absorption and Its Radial Distribution

It was noted by Clark and McCord (1980) and Clark *et al.* (1984) that the spectrum of the rings seemed to show a weak absorption feature in the 850-nm spectral range. Such a feature is not uncommon in the spectra of other icy objects (Calvin
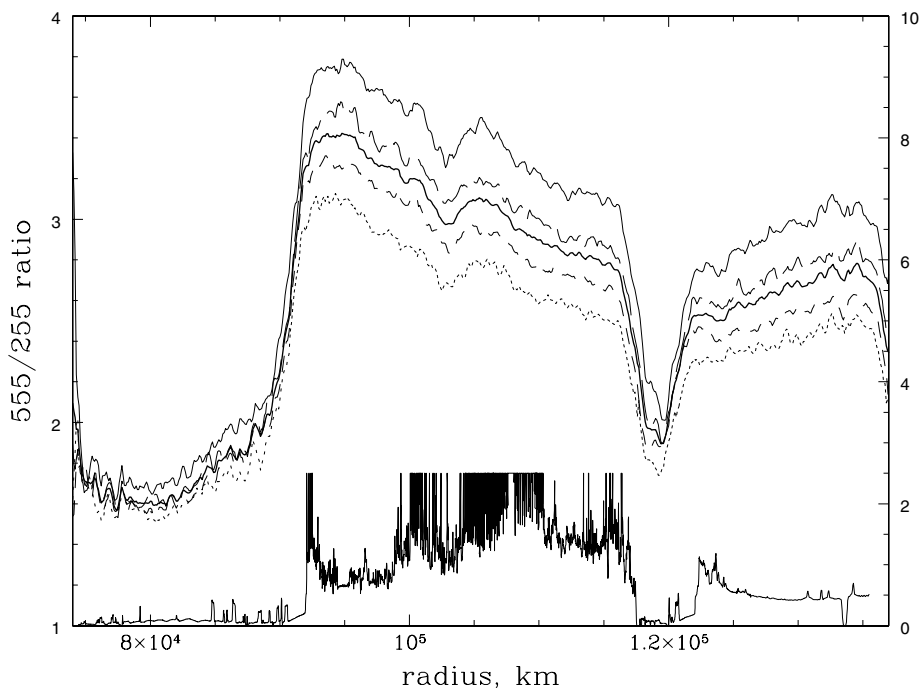
FIG. 13. Radial profile of F555W/F255W color ratios. Light weight lines: individual profiles obtained at phase angles $\alpha = 0.3°$ (dotted), $0.7°$, $2.0°$ (long dash), and $6.3°$ (solid). Heavy solid line: average of all these individual profiles. Radial variations in the ratio are discussed in Section 3.5. The optical depth profile at the bottom, saturating at around $\tau = 2.5$, is from Voyager ISS data as noted in Fig. 12.
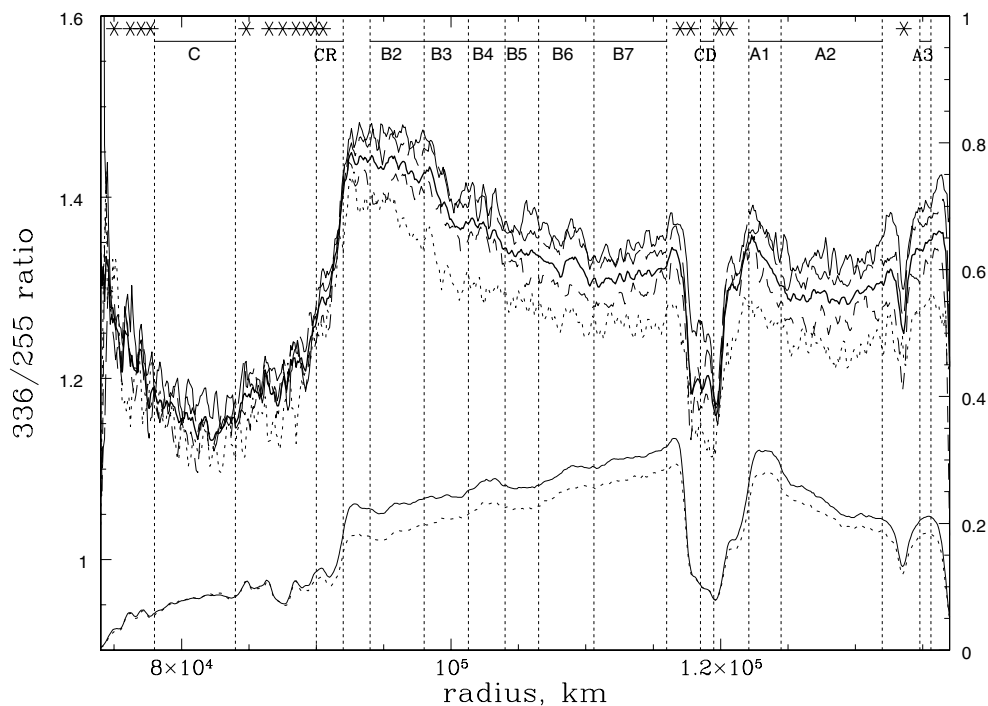

FIG. 14. F336W/F255W ratios as functions of radius and phase angle. Solid: $\alpha = 6°$; long dash: $\alpha = 2°$; short dash: $\alpha = 0.7°$; dotted: $\alpha = 0.3°$. The heavy solid curve is the average of all four ratio profiles shown. Shown at the bottom are I/F profiles in the F255W filter (dotted) and the F336W filter (solid, scaled down by 0.86 to normalize the C ring reflectivities and emphasize regional differences).
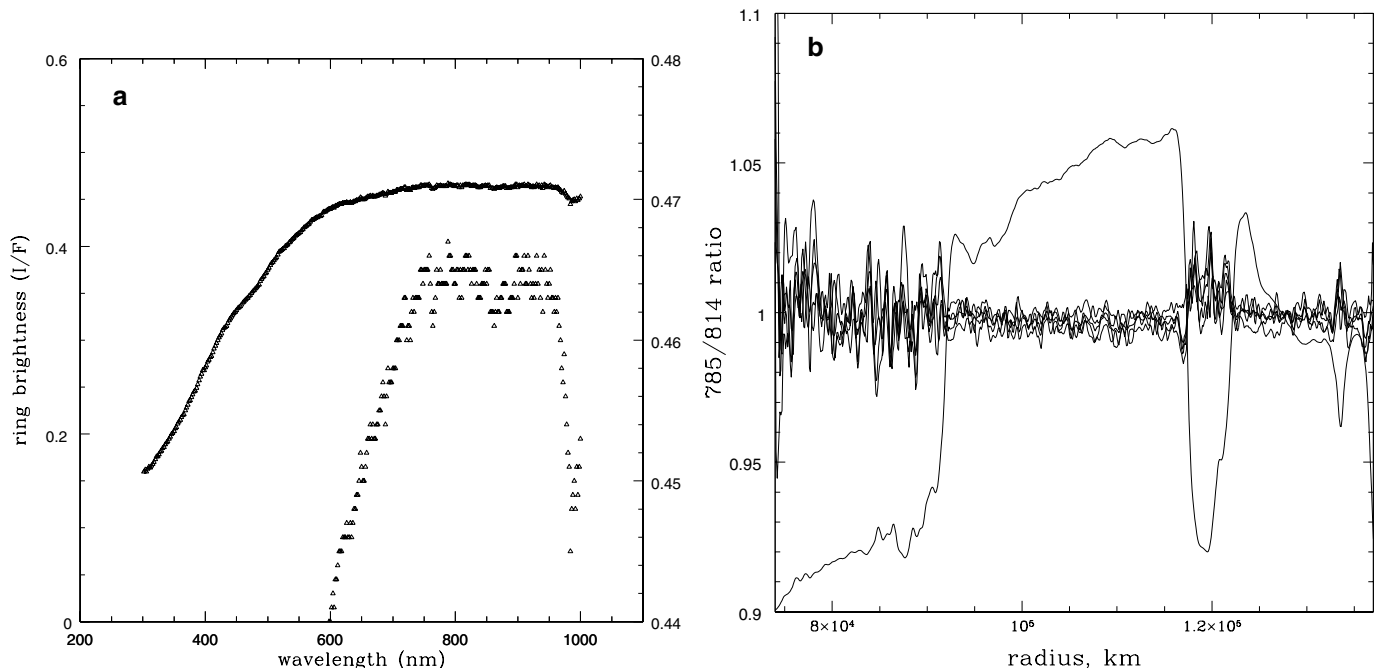
FIG. 15. (a) Average ring spectrum from Karkoschka (1994), both at normal scale (left) and vertically stretched (right). While not mentioned specifically by Karkoschka (1994), it appears to us that this spectrum supports the reality of a possible weak 850-nm absorption as noted by Clark and McCord (1980) in ring average spectra. (b) Radial profile of F785LP/F814W reflectivity ratio, averaged over our five three scans (Table III) except in the middle and outer B ring, where one scan is saturated and the average contains only four scans. There is no clear evidence for regional variation in this ratio, and therefore in the relative strength of the putative 850-nm absorption feature. Also shown: ring I/F in the F785LP filter (right scale).

et al. 1995) and is usually attributed to Fe^{3+} present in the lattice (e.g., Morris and Golden 1998). Clark (personal communication, 1999) indicated a continuing belief in the reality of the feature, although he suspected that it might be weaker than apparent in the Clark and McCord (1980) spectrum. Inspection of the slit spectrum of Karkoschka (1994) also seems to support a weak feature in the 850-nm spectral region (Fig. 15a).

In an attempt to ascertain the presence or absence of 850-nm absorption, we have obtained several images in the F785LP filter, whose bandpass is a fairly good match for the location of this feature (see Fig. 2). Of course, as discussed in Section 2, anyone would be reluctant to accept spectral variations in intensity alone at the percent level because of calibration uncertainty in the various HST passbands. Instead, we tried constructing radial profiles of the ratio of intensity "in" and "out" of the putative spectral feature. Calibration problems cannot produce radial variations in such reflectivity ratios—but real radial variations in the abundance of 850-nm-absorbing ring material could. This approach tests the hypothesis that there *is* an 850-nm absorber *and* it is radially heterogeneous.

In Fig. 15b, we present radial ratio profiles obtained from the five best F785LP and F814W image pairs. One image pair taken at the lowest (4°) opening angle was not used due to larger noise and more uncertain scattered light background, to which C ring ratios are especially sensitive. One of the F785LP images was saturated in the B ring (103,000–117,000 km), so the data shown by the heavy line of Fig. 15 are averages from only two image scans within that range of radii. There is no evidence for

regional radial variation of the F785LP/F814W reflectivity ratio at the percent level.

The ratio profiles are sensitive to uncertainties in the PSF, and small changes in the slope of the PSF between these two filters can cause the F785LP/F814W reflectivity ratio to be a few percent larger, or a few percent smaller, in the C ring than in the B ring. It might be that an incorrect selection of PSF halo functions has obscured actual regional differences, but if so they must be at a level of only a percent or so. That is, after doing the best job we can at deconvolving the scattered light, and exploring a range of subtly varying PSF power law halo functions, we believe we can say that the PSFs used for deconvolving these data (Table II) are distinctively better than either steeper or flatter PSFs which change the C ring F785LP/F814W ratio by only 2%. The C ring is more sensitive than the B ring because of its low reflectivity. Thus, we cannot provide evidence for the presence or absense of an 850-nm absorber from the HST data and, in fact, suspect that regional differences in the strength of this absorption are probably at the percent level or less.

We note that there is no discernible phase dependence of the F785LP/F814W color ratio between phase angles of 0.3° (light dotted curves) and 1.0° (light solid curve).

3.3.4. 1042-nm Absorption?

Finally, we obtained ratio profiles from three pairs of F1042M and F814W images (Fig. 16). This was motivated partly on the possibility of a water-band related downturn possibly evident at
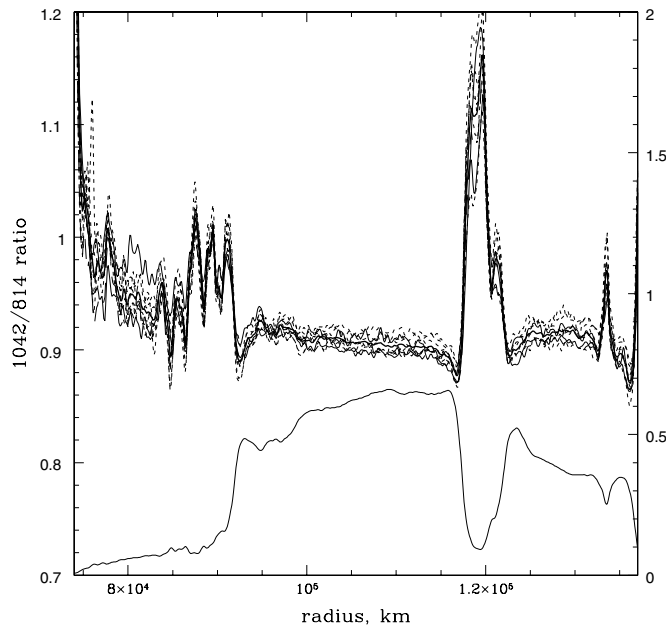
FIG. 16. Radial profile of F1042M/F814W color ratios obtained at phase angles $\alpha = 0.4$ and $0.5°$ (dotted), $1.2°$ (dashed), and $6°$ (solid). Note that, in contrast to the strong and systematic phase variation of the F555W/F336W, F555W/F255W, and F336W/F255W color ratios, the five profiles are in good agreement and there is no systematic color variation with phase angle. As discussed in Section 3.3.4, we believe the strong variations in the outer C ring and Cassini Division, as well as at the A and B ring edges, are artifacts of incomplete correction. Also shown: radial profile of ring I/F (right scale).

the long wavelength end of Karkoschka's slit spectrum (Fig. 15a). Increased absorption at this wavelength (near the 1.04 μ water ice band) might be caused by an increased area coverage by water ice or with locally larger grain sizes (e.g., Geissler *et al.* 1995, 1997). However, recently Karkoschka (personal communication, 2001) has indicated that a decreasing signal-to-noise ratio at the long wavelength end of his reflectivity spectrum puts this fine-scale spectral structure at wavelengths longer than 960–980 nm into considerable doubt.

Distinguishing real variations from artifacts in these profiles is difficult. One feature that leaps to the eye is that the Cassini Division and outer C ring particles have a relatively large ratio of F1042M/F814W reflectivity. We have decided that these apparent regional differences cannot be distinguished from artifacts which might be produced by the greatly different PSFs in these two filters—especially in the F1042M filter. As seen in Fig. 5, the F1042M is qualitatively different from the others. It is the one filter where the STScI staff believes the Tiny Tim software really treats the halo correctly, so we have retained the nominal Tiny Tim PSF instead of selecting it interactively as that which best removes the scattered light inside the C ring, as we did for all the other cases. However, the correction functions shown in Fig. 4 show that local maxima occur in the outer C ring and the Cassini Division exactly where the radial profile of F1042M/F814W reflectivity in Fig. 16 has maxima. This suggests that contamination remains in the form of light

scattered into the Cassini Division and inner C ring from adjacent, much brighter regions, in amounts that are perhaps twice our estimated correction function. Other apparent "dips" in the F1042M/F814W ratio near sharp A or B ring edges could result from undercompensation of 1042nm light scattered *out* of these regions into surrounding regions.

The F1042M/F814W ratio is certainly less radially variable across the regional boundaries (C ring/B ring) where other spectral regions show substantial variability. As with the F336W/F255W ratios, but unlike the F555W/F336W ratios, no intermediate scale structure is seen in the B ring. There is a very subtle difference in the inner, less optically thick, quarter of the B ring relative to the outer B ring, which is perhaps only a weaker version of the artifact seen in the outer C ring due to the adjacent brighter middle B ring. As emphasized in the case of the F785LP (850-nm) absorption, we feel radial structure in ratios, which avoids calibration uncertainties, is more sensitive to compositional variation than slight differences in spectra, and we place little weight on the observed 5–6% absolute difference between the I/F's in the F1042M and F814W filters.

The main point of interest here may be that the F1042M/F814W color ratios, like the F785LP/F814W ratios, are independent of phase angle (the five geometries from which these ratios were formed had phase angles $\alpha = 0.4$–$0.5°$, $1.2°$, and $6.0°$). This distinction between phase-independent color ratios in the >700-nm spectral range (Figs. 15 and 16) and phase-dependent ratios in the 255–600-nm spectral range (Figs. 10–14) is directly connected to the spectral slope in the spectral ranges involved, as discussed further below and in Section 4.1.

3.4. Regionally Averaged Spectra

Figure 17 shows the averaged spectra for the regions described in Section 3.1 and shown in Figs. 6 and 7. As has long been known, the rings have a steep reflectivity gradient between 300 and 600 nm and are relatively constant in reflectivity at longer wavelengths. For instance, the slit spectrum of the entire averaged ring system by Karkoschka (1994) is shown in Fig. 15a. Some previously published data (reviewed by Clark *et al.* 1984) show a clear downward trend for the ring reflectivity for wavelengths longer than 600 nm. Clark now believes (personal communication, 2000) that this trend might be an artifact of an incorrect lunar reference spectrum, and that the average spectrum might well be flat through most of this spectral range. Because we have found the ring colors to be phase-angle dependent (Section 3), the spectra are shown for two different phase angles ($\alpha = 0.6°$ and $6.0°$) and a standard opening angle of $-15°$. Observations with the F785LP or F1042M filters are not obtained at every visit, so the F1042M or F785LP reflectivities were ratioed to the F814W reflectivity *on the same* visit/phase/opening and these ratios were then applied to the F814W reflectivities at the standard phase angles of $\alpha = 0.6°$ and $6°$ (see Tables I and III for precise values of geometrical parameters).

A more sensitive comparison between the shapes of the normalized spectra is shown in Fig. 18. The differences between
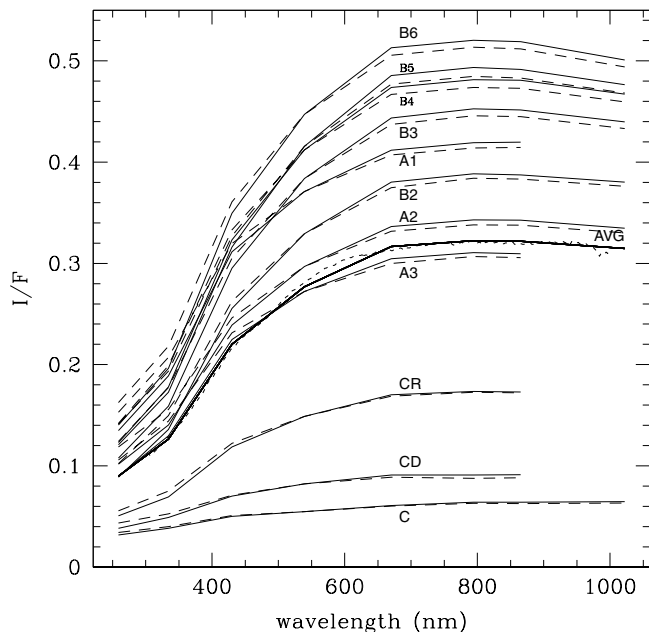
FIG. 17. Ring spectra for the different regions defined in Table IV. All spectra are in actual I/F units for an opening angle of approximately $-15°$. Dashed curves: $\alpha = 0.6°$; solid curves: $\alpha = 6.0°$. Note the increase in redness between $0.6°$ and $6.0°$ phase angle. The curve labeled "average" is weighted only by ring radial bins and is suitable for comparison with the ring average slit spectra of Karkoschka (1994, dotted line). The F1042M points are not plotted for the regions CR, CD, A1, or A3 because we believe that uncorrected scattering is biasing their value upward or downward (see Sections 3.3.4 and 3.4).
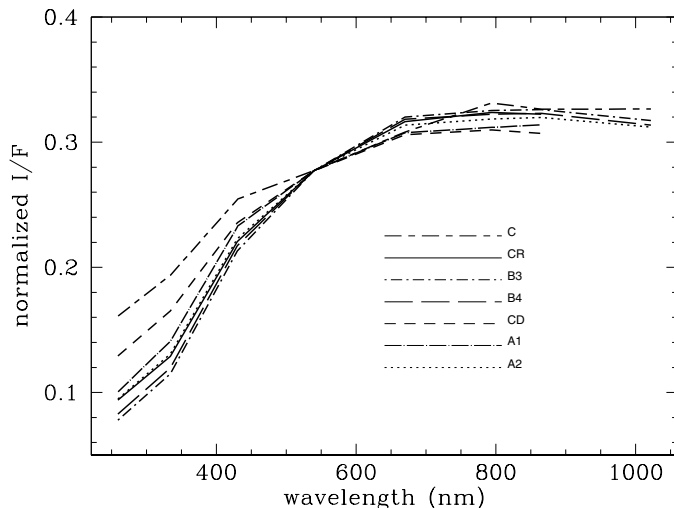

FIG. 18. Ring spectra at $\alpha = 6.0°$ for a subset of the ring regions, normalized at F555W to the ring average spectrum. Note how subtle the differences in shape are between the A and B ring regions. Regions B2, B3, and B5 are even more similar in shape so only B3 is shown; also, regions B4 and B6 are so similar that only B4 is shown. The F1042M points are not plotted for regions CR, CD, A1, or A3 because we believe that uncorrected scattering is biasing their value upward or downward (see Sections 3.3.4 and 3.4).

these regions are real, but subtle. Only the F1042M points are under some suspicion near ring edges (in fact, the F1042M points are not plotted for regions CR, CD, A1, and A3 where they are suspect). Two features are worthy of note: (a) the unusual lack of concave downward curvature for the middle C ring (C) spectrum in the F555W and F675W passbands speaks for a relatively large amount of material there to absorb these wavelengths, and (b) the continued rise in reflectivity of region C toward F1042M, compared to the decrease toward F1042M in the "icier" rings A and B. In the regions shown, no PSF-related scattered light artifacts are suspected, so this difference may be real (it is also seen in the unnormalized spectra of Fig. 17).

4. DISCUSSION AND IMPLICATIONS

4.1. Phase Variation of Ring Color—Particle Regolith Effect or Facet Illumination of Shadows?

There has been little discussion in the literature of significant phase reddening of icy outer Solar System objects within the range of phase angles accessible from Earth. Our color ratios between 336 and 555 nm should be compared with $U - V$ magnitude differences. Franklin and Cook (1965) found Saturn's ring to redden in $B - V$ at the rate of 0.013 mag/degrees between $0.5°$ and $2°$ phase angle, but found no reddening to larger phase angles. The phase reddening in our F555W/F439W results, the actual analog to the Franklin and Cook $B - V$ results, is only 0.008 mag/degrees, consistent with the results of Franklin and Cook (1965) at the level of accuracy of the observations. However, our results show that about half of this occurs between $2°$ and $6°$, while Franklin and Cook (1965) seem to show the reddening to cease for phase angles greater than about $1°$. These do not seem like serious discrepancies in view of the fact that their intensity calibration relied on various atmospheric regions on the planet. However, our F555W/F336W reddening results (corresponding to $U - V$ colors) of 0.05 mag/degrees between $0.5°$ and $2°$, and 0.024 mag/degrees between $2°$ and $6°$ phase angle, are considerably larger.

Concerning other icy objects, the tables in Noland *et al.* (1974) imply reddening in the Johnson $u - y$ system (comparable wavelengths to standard $U - V$) for Rhea, Dione, and Tethys of slightly less than 0.02 mag/degree but except for Rhea, these amounts are only slightly larger than their error bars. Lumme and Bowell (1981) found the Galilean satellites to have no phase reddening in $U - B$ and $B - V$ within their measurement errors (see b_1 and u_1 of their Table VI). Hendrix *et al.* (1998) compare their Europa phase curve at 290 nm with phase curves by Domingue and Hapke (1992) which show a phase reddening of 0.3% over $\alpha = 0 - 10°$—far smaller than the 14% effect shown by the B ring over this range of α.

Data on Io presented in Gradie and Veverka (1986) seem to imply a small phase reddening Io in $U - V$ colors of about 0.006 mag/degree between $4°$ and $60°$ phase angle. Simonelli and Veverka (1986) used Voyager observations between $2°$ and

5° phase angle to derive phase coefficients in the G and UV filters. The "average" regions have G filter phase coefficients around 0.03 ± 0.01 mag/degree; unfortunately, the corresponding UV phase coefficients are rather scattered (0.04 ± 0.04 mag/degree). For the "bright" regions, the UV phase coefficients are the most well defined at 0.04 ± 0.02 mag/degree and the G filter phase coefficients are around 0.015 ± 0.07 mag/degree. The difference, or phase reddening, for the bright regions is thus around 0.025 ± 0.02 mag/degree. While this effect, if indeed real, is comparable to what we find over the same range of phase angle, Io is also both brighter and redder than the rings, so the comparable magnitude of the rings' phase reddening would still seem somewhat unusual.

Some interesting conclusions can be drawn from the HST data set alone, as well as from the combination of the HST and Voyager observations. First, the wavelength range between 255 and 600 nm, where the overall ring reflectivity varies dramatically (cf. Fig. 17), shows phase angle variation (Figs. 10–12) whereas the wavelength range between 600 and 1000 nm—a comparable factor in wavelength where the overall ring reflectivity is nearly constant—does not (Figs. 15 and 16). This indicates that the varying G/UV color ratio is not a particle-size-dependent effect, which comes as no surprise based on current knowledge that the vast bulk of the ring particles are much larger than visual wavelengths. It also implies an increased role for multiple scattering of *some* kind with increasing phase angle, because red regions increase in redness with phase angle.

Second, the geometrical dependence of color variation is confined almost entirely to *phase angle*, and almost lacking with *opening angle*; compare, for instance, the well-separated families of dotted, dashed, and solid curves in Fig. 11. It is especially obvious that there is no discernible reddening with opening angle in the A ring and inner B ring.

If *interparticle* scattering were more important, one would expect the color ratios to increase as the rings opened up and sunlight could better penetrate the rings. These arguments are quantified in the Appendix. While the slightly larger spread between the color ratios in the B ring at different opening angles seen in Fig. 11 might be partly due to a small multiple interparticle scattering contribution, the overall lack of opening angle dependence tends to indicate that even at opening angles as large as $B = 20°$, much of the ring layer can be treated as single-ring-particle scattering from ground-based geometries. In fact, radiative transfer (doubling) calculations show the multiple scattering contribution in these geometries, for expected particle phase functions, is in the 2–5% range (Cuzzi *et al.* 1984, Dones *et al.* 1993). All these arguments support the interpretation that multiple interparticle scattering plays no role in determining (at least) the A and B ring color ratios and reflectivities.

For these reasons, we believe the data argue for multiple scattering *within* the regoliths of individual ring particles, rather than *between* independent ring particles in a classical scattering layer. In view of these arguments, the strong *phase angle* depen-

dence of color can only be explained if the phase functions of *individual ring particles* are wavelength dependent. Combined with the fact that the phase angle dependence of color ratio is associated with wavelength regimes where the overall particle color changes, this leads us to an explanation for the phase function variation which involves multiple scattering in the regolith and/or multiple scattering between facets into shadows. That is, if the regolith grains become better scatterers with increasing wavelength because of lower material absorption coefficients (Cuzzi and Estrada 1998), the degree of internal multiple scattering increases and the angular distribution of emergent photons becomes broader. Or, if the particle surfaces are brighter at longer wavelengths, they will more effectively illuminate the shadows which are increasingly visible at larger phase angles. Both explanations need to be modeled quantitatively (Poulet *et al.* 2000, 2002).

Unfortunately, uncertainties which remain in the Voyager color calibration (primarily in the sensitivity of the Voyager 2 UV filter; Estrada and Cuzzi 1996; Estrada *et al.*, in preparation) limit its usefulness. Since other analyses (Cooke 1991, Dones *et al.* 1993; Poulet *et al.* 2000, 2002) suggest that the phase function, and thus the reddening, will vary across the ring, it is not clear if there is a single scaling factor which can reconcile the HST and Voyager data. This is clearly an uncertainty that we are not in a position to resolve without Cassini data.

Finally, the color-dependent $P_\lambda(\alpha)$, combined with the calibration error in the Voyager 2 colors of Estrada and Cuzzi (1996), invalidate some of the conclusions of Cuzzi and Estrada (1998). While the B ring remains redder than any of Saturn's moons, the C ring does not seem to be. The quantitative inferences of Cuzzi and Estrada (1998) regarding the abundance and refractive indices of non-icy ring constituents will have to be reassessed. However, the overall conclusions of Cuzzi and Estrada (1998) regarding the good fit of compositional evolution models based on meteoroid bombardment, including the simple qualitative explanation of the correlation of color and ring optical depth/mass density, the good fit of the radial profile of color "bleeding" across the inner edges of the B ring, and the conclusions regarding the short exposure age of the rings, probably remain valid.

4.2. Ring Vertical Structure: Classical or Nonclassical?

Recall from Fig. 8 that the C ring, mid A ring, and even inner B ring for most opening angles are fairly well modeled by a classical, many-particle-thick, single scattering layer, while the outer B ring shows considerable deviation from this behavior. The arguments against a substantial role for multiple scattering imply that this deviation from predictions is due to local deviation of the ring layer in optically thick regions from a many-particle-thick configuration. Dones *et al.* (1993) had previously reached similar conclusions for the optically thick regions of the inner A ring, at least, based on the inability of many-particle-thick

models to predict observed optical depth-dependent reflectivity variations for optical depths larger than 0.5 or so. Recent models by Salo and Karjalainen (2001) and Porco *et al.* (2001) confirm these early indications.

4.3. Compositional Variations within the Rings

F555W/F336W reflectivity, color, and optical depth. Estrada and Cuzzi (1996) noted the unusually red bands lying in the inner and middle B ring at radii of 98,900–101,000 km (here denoted as region B2). Figures 10–12 show these bands in the smoothed Voyager scans as well as in the HST ratio plots at the same wavelengths. Perusal of the original Estrada and Cuzzi (1996) plots shows these to be more intense and more noticeable than other color features in the B ring, but they are relatively narrow, and at the lower resolution of the HST data, they look no more prominent than another reddish region lying outside of 104,000 km (region B5). Figure 19 shows that both of these relatively red regions correlate fairly well with optically

thick regions. Note that the prominent dip in optical depth and F555W/F336W color ratio in region B4, and the adjacent outer red band, is quite evident in the F555W/F255W ratio as well (Fig. 13) although the inner red bands seem muted or absent. Comparison across the panels of Fig. 19 indicates that regions B4 and B6, both relatively high in reflectivity, share a relatively low ratio of F555W/F336W reflectivity. However, region B3 is a local minimum in optical depth and the center of the color dip in region B6 (109,000 km) is not any kind of optical depth extremum (cf. Esposito *et al.* 1984, Fig. 2). With the exception of the 109,000-km color dip, the relatively "red bands" of regions B3 and B5–B6 do tend to correlate with optically thick regions. In addition, there is an overall reddening, or increasing F336W absorption, inward across the entire B ring.

Far-UV absorption (Section 3.3.2). The ring spectrum varies in similar, but subtly different ways between the closely spaced F255W and F336W filters (Fig. 14). Note that the inner B ring red bands (100,000 km) are not at all evident in this color ratio, implying that the large optical depth fluctuations in that region
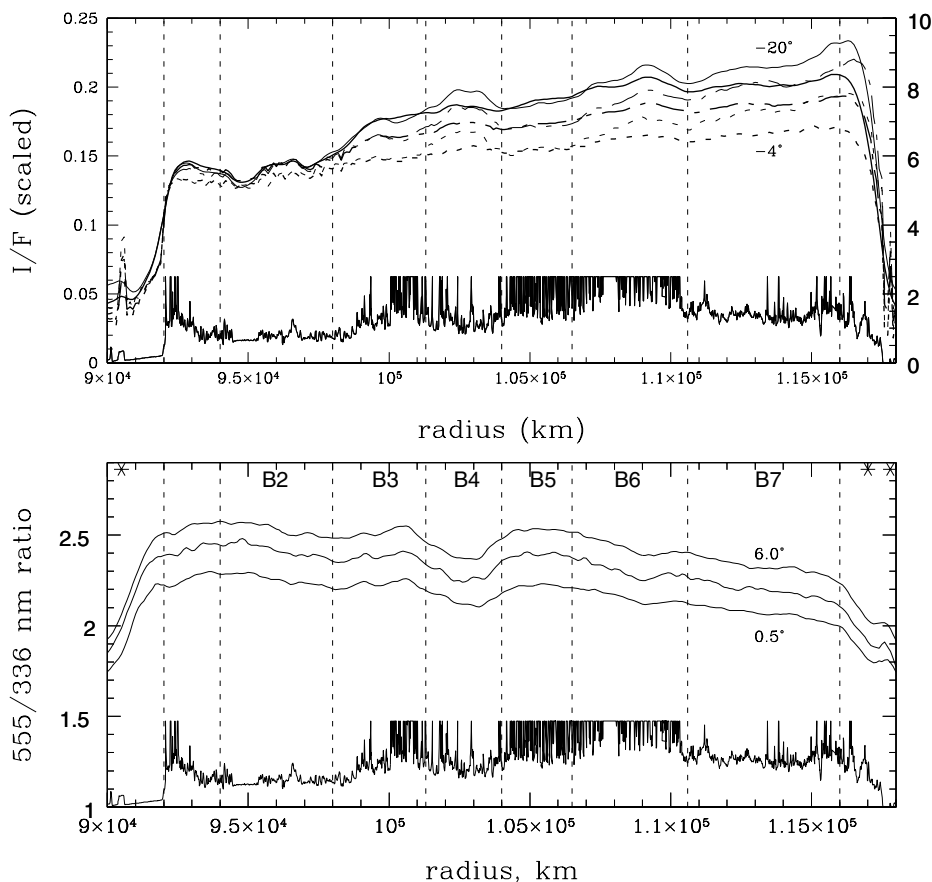

FIG. 19. This figure focuses on the B ring regions defined in Table IV, illustrating how the variations in reflectivity, color ratio, and optical depth contribute to their definition. The upper panel is a magnification of data presented in Figs. 8b and 8c, normalized to overlap in the inner B ring region. The light lines are from F336W and the heavy lines are from F555W. Profiles from three-ring opening angles are shown (−4°, −10°, and −20°). In the lower panel are the profiles from Fig. 12, averaged over tilt angles at $\alpha = 0.5°$, 2.0°, and 6.0°.

are not a determinant of differential F255W/F336W absorption, as they are for F336W/F555W absorption. This in itself is evidence for several different populations of material (Cuzzi *et al.* 2000)—one population that is correlated with underlying optical depth (as manifested in ratios between F555W and shorter wavelengths) and at least one population that is not (as manifested in these UV ratios).

The differential absorption of Fig. 14 may be interpreted in different ways—as increased F336W absorption in the C ring and Cassini Division, or as increased F255W absorption in the A and B rings. In the reflectivity profiles at the bottom of Fig. 14, the dotted F255W profile has been scaled upward to align with the F336W profile in the C ring and Cassini Division as if the latter were the case. It appears that the difference between F255W and F336W consists of a constant decrement in F255W reflectivity, which translates into the variable curved profile when divided by the increasing overall reflectivity. Weak features can be discerned in regions B3 (local minimum of F336W/F255W) and B6 (local maximum of F336W/F255W). These anticorrelate with the local minima in F555W/F336W seen in Fig. 18.

Clearly, regional spectral variations are complex and will not be simply or quickly explained. A more powerful approach to identifying and studying regional spectral variations is a principal components/cluster analysis approach, as reported by Cuzzi *et al.* (2000) and in which very complex radial variations are seen which correlate with both radius and optical depth. This approach will be pursued more in a future publication.

Possible constituents responsible for far-UV absorption. The overall redness of the rings has been known, without generating much comment, for decades (Lebofsky *et al.* 1970). Organic material was suggested by Cuzzi and Estrada (1998) as the primary reddish colorant for the main rings based on Voyager UV–V–G photometry (note, however, that these results need to be quantitatively redone in light of the revised Voyager colors). In addition to this overall reddish material, our HST data may provide evidence for different material which absorbs in the far-UV spectral range, with a different radial distribution. This is because the radial profiles for 336/255 absorption shown in Section 3.3.2 are *qualitatively different* than the overall profiles of 555/336 absorption—not just "more of the same."

With our spectral resolution, we can not distinguish between the various possibilities of SO_2 or sulfur (Ockert *et al.* 1987, Hendrix *et al.* 1998, Lane *et al.* 1981, Fanale *et al.* 1999), O_3 (Noll *et al.* 1997), or any of a number of abundant ices which have steep absorption edges in the UV between 320 (SO_2), and 230 nm (NH_3, H_2O) (Hapke *et al.* 1981). We also note that Jenniskens (1993) shows that the absorptivity of several organic refractory residues continues to increase dramatically between 300 and 100 nm, but in a fairly smooth fashion except for one sample that is actually *more* absorbing in the 336-nm region than at shorter wavelengths. IUE spectra (Wagener and Caldwell 1986, 1988) detect the 170-nm ice absorption edge in the

rings, but there is no evidence for any other features in the 170–300-nm spectral range. The 170-nm edge itself is at too short a wavelength to have any effect on the F255W filter intensities, and an abrupt edge anywhere at longer wavelengths seems impossible to reconcile with the IUE spectra. For instance, a complete edge at 236 (240) nm would produce a 7% (16%) relative darkening at F255W. Such a feature would be clearly visible in the IUE spectra which extend to 300 nm.

It *might* be possible to shoehorn some form of spectral reflectivity gradient in just longward of the long wavelength limit (300 nm) of the IUE spectrum of Wagener and Caldwell (1986) and just shortward of where it would begin to affect the F336W filter. In fact, a muted version of this sort of behavior does seem to be found on the surfaces of Dione and Rhea (Noll *et al.* 1997), which (in the noisier IUE data) would probably look spectrally flat between 200 and 300 nm, and begin to brighten quickly longward of 300 nm consistent with the existing IUE spectra of the (primarily B and A) rings. Noll *et al.* (1997) also show spectra for Iapetus which do not show the relative absorption in the 200–300 nm range, presumably because other absorbers are active longward of 300 nm; Iapetus might be a good analog for the C ring and Cassini Division.

In addition, or instead, the C ring and Cassini Division material might contain a relatively large abundance of some 336 nm absorbing material relative to the B and A rings. In the context of the compositional evolution model of Cuzzi and Estrada (1998), this would simply imply that the extrinsic "polluting" material contains more of the 336-nm absorber than the intrinsic material, and if so would imply that the extrinsic material is considerably more absorbing at 336 nm than at 255 nm, to explain the low F336W/F255W ratio in the C ring.

5. SUMMARY

Based on phase and opening angle variations of color ratios, and comparison with theoretical predictions, we find that the C ring, Cassini Division, inner B ring (at most opening angles), and much of the A ring can be adequately described by single scattering in a classical, many-particle-thick layer over the range of geometries observable from Earth. Over spectral regions where the rings are red, the redness increases with increasing phase angle but is independent of ring opening angle. We argue that this is understandable in light of multiple scattering within the regoliths or surface facets of individual ring particles, but not between independent ring particles in a vertically extended, classical scattering layer. This issue is studied in detail by Poulet *et al.* (2000, 2002).

Color features in the middle B ring seem to correlate better with the high optical depth structures which are found there than do reflectivity variations, and these associations might indicate "source" or "reservoir" regions in some sense. Qualitatively different F336W/F255W color ratio profiles show less (or no) evidence for consistent color differences associated with these optical depth structures.

The fact that structure in the color ratio profiles is qualitatively invariant even as the overall color varies with phase angle implies that these radial features represent real variations in the composition of the underlying material. It seems plausible to us that the rather different radial structure of the profiles of color ratio between different wavelengths is indicative of the presence of a number of compositionally distinct materials within the rings, each with different radial distributions. The story of the nature of Saturn's rings is not all black and white.

APPENDIX

Classical work of Lumme and Irvine (1976), Esposito and Lumme (1977) and Lumme *et al.* (1983) concluded that multiple interparticle scattering played an important role in the ring brightness. The earliest data were obtained by Lumme and Irvine (1976), who scanned ground-based photographic plates from four different observatories with microdensitometers. Lumme and Irvine (1976) had to deal with the complications of atmospheric and instrumental smearing (which are more serious at low opening angle than at large opening angle, leaving room for systematic errors) as well as variable calibration (all reflectivities are given relative to that of the disk center, which varies in latitude with time and might be subject to temporal and zenith angle variations as well). The extensive correction process which attempts to account for all these factors is documented in Lumme and Irvine (1976) and the equally thorough Lumme *et al.* (1983). These papers took extreme care to extract the maximum amount of information from the data they had available.

Indeed, some of the things they observed are confirmed qualitatively, if not quantitatively, by our data even though their radial brightness distribution (e.g., Lumme and Irvilne (1976), Fig. 7) bears only a faint resemblance to the actual distribution. It is indeed true that the brightness of the B ring increases faster with opening angle than can be accounted for by single scattering in a classical, many-particle-thick layer (Fig. 8). The real issue is, to what cause can this increase be attributed? Lumme and Irvine (1976) and subsequent workers were able to find combinations of particle albedo, phase function, and ring optical depth which, in the context of a classical, many-particle-thick ring, produced multiple scattering contributions consistent with the observed brightness increase.

However, other "classical" results are inconsistent with the HST data; specifically, our finding that the rings become significantly redder with increasing phase angle (Fig. 10). None of the extensive phase studies of Lumme and Irvine (1976), Lumme *et al.* (1983), or Cook and Franklin showed any evidence for phase reddening. We checked the analytical fits of Lumme *et al.* (1983) (their Table IIa) for four different apparitions and the reddening (0.59–0.42 microns) is perhaps at the 1–3% level. Our color variations (0.55–0.34 microns) are at the 14% level, nearly an order of magnitude larger, and are repeatable at a range of tilt angles. Furthermore, the HST data show that this phase-dependent ring color is essentially independent of ring opening angle (Fig. 11). There is at most a 5% tilt effect on color, and that allowable only at the largest phase angle; the data are consistent with no effect at all given the uncertainties. The newly discovered combination of phenomena—phase reddening without tilt reddening—argues against the classical interpretation, and in fact argues that multiple interparticle scattering is negligible everywhere (at the few percent level) in Earth-based geometries.

The following calculation indicates the degree of difficulty a purely multiple scattering model would have explaining simultaneously the increasing ring brightness and invariant ring color. Suppose the singly scattered intensity $I_1(\lambda)$ has spectral slope $R_1 \approx \varpi(\lambda_2)/\varpi(\lambda_1)$, where ϖ is the single scattering albedo at wavelength λ. We neglect the small variation in angular scattering behavior for macroscopic particles with grainy surfaces over this small range of phase angles; it is certainly unimportant for the multiply scattered component (Lumme and Irvine 1976, p. 880). The spectral slope of the multiply scattered light is thus $R_M \approx (\varpi(\lambda_2)/\varpi(\lambda_1))^n$, where n is the typical order of scattering and $n \sim 2$–3 perhaps, for large, backscattering particles. Then the

slope of the total intensity is just $R_T \approx f_1 R_1 + f_M R_M$, where f_1 and f_M are the fractions of singly and multiply scattered light, respectively. We use the notation of Lumme and Irvine (1976), where $q = I_M/I_1$; then $R_T \approx (R_1 + q R_M)/(1 + q)$. Substituting $R_M = R_1(\varpi(\lambda_2)/\varpi(\lambda_1))^{n-1}$, we find $R_T/R_1 = (1 + q(\varpi(\lambda_2)/\varpi(\lambda_1))^{n-1})/(1 + q)$. Given that all models show single scattering to predominate, we can take $\varpi(\lambda_2)/\varpi(\lambda_1)$ as the spectral ratio to first order (Fig. 17 or Fig. 18). Consider ring segment B6, the central part of the region which exhibits anomalous tilt brightening. The brightness ratio $\varpi(\lambda_2)/\varpi(\lambda_1) = 0.45/0.21 \sim 2$, where $\lambda_1 = 336$ nm and $\lambda_2 = 550$ nm. Suppose we adopt the results of Lumme *et al.* (1983), where $q = 0.25$ at the highest opening angle (their Fig. 3); assuming $n \approx 2$–3, we would then expect the ring color to redden by a factor of $R_T/R_1 = (1 + 0.25(2)^{1-2})/1.25 \approx 1.25 - 1.75$, which is not compatible with the observed lack of tilt reddening at our observed few percent level (Fig. 11). In fact, this simple calculation underestimates the expected magnitude of the multiple scattering effect, because it assumes the degree of multiple scattering (the factor q) is the same at both wavelengths, while it would surely be less at the shorter wavelength where the albedo is smaller.

Instead, it was our conclusion (Sections 3.2 and 4.2) that the increasing brightness of (the outer two thirds of) the B ring is due *not* to increased multiple interparticle scattering, but instead to nonclassical layer effects. It has been known for some time that many, if not all, brightness fluctuations seen in the optically thickest parts of the main rings are not explainable in terms of optical depth variations in a classical layer (Dones *et al.* 1989, 1993). In fact, dynamical expectations lead us to believe that optically thicker layers, where collisions are more frequent, might have different (more condensed) vertical structure than classical layers. Recent photometric modeling by Salo and Karjalainen (2001) appears to verify that denser layers exhibit the expected behavior.

ACKNOWLEDGMENTS

REFERENCES

Baggett, S., and S. Gonzaga 1998. *WFPC2 Long-Term Photometric Stability*. Instrument science report WFPC2 98-03. Space Telescope Science Institute, Baltimore.

Biretta, J. 1996. *WFPC2 Instrument Handbook*, version 4.0. Science Support Division, Space Telescope Science Institute, Baltimore.

Bohlin, R. C., L. Colina, and D. S. Finley 1995. White dwarf standard stars: G191-B2B, GD 71, GD 153, HZ 43. *Astron. J.* **110**, 1316–1325.

Bosh, A. S., and A. S. Rivkin 1996. Observations of Saturn's inner satellites during the May 1995 ring-plane crossing. *Science* **272**, 518–521.

Caldwell, J. 1975. Ultraviolet observations of small bodies in the Solar System by OAO-2. *Icarus* **25**, 384–396.

Calvin, W. M., R. N. Clark, R. H. Brown, and J. R. Spencer 1995. Spectra of the Galilean satellites from 0.2 to 5 μm: A compilation, new observations, and a recent summary. *J. Geophys. Res.* **100**(E9), 19,041–19,048.

Casertano, S. 1997. WFPC2 photometric calibration. In *The 1997 HST Calibration Workshop with a New Generation of Instruments* (Stefano Casertano, Robert Jedrzejewski, Charles D. Keyes, and Mark Stevens, Eds.), pp. 327–337. Space Telescope Science Institute, Baltimore.

Chandrasekhar, S. 1960. *Radiative Transfer.* Dover, New York.

Clark, R. N. 1980. Ganymede, Europa, Callisto, and Saturn's rings—Compositional analysis from reflectance spectroscopy. *Icarus* **44**, 388–409.

Clark, R. N., and T. B. McCord 1980. The rings of Saturn: New near-infrared reflectance measurements and a 0.326–4.08 μm summary. *Icarus* **43**, 161–168.

Clark, R. N., F. P. Fanale, and M. J. Gaffey 1984. Surface composition of natural satellites. In *Satellites* (J. A. Burns and M. S. Matthews, Eds.), pp. 437–491. Univ. of Arizona Press, Tucson.

Colina, L., R. C. Bohlin, and F. Castelli 1996. The 0.12–2.5 micron absolute flux distribution of the sun for comparison with solar analog stars. *Astron. J.* **112**, 307–315.

Cooke, M. 1991. *Saturn's Rings: Photometric Studies of the C Ring and Radial Variation in the Keeler Gap.* Ph.D. thesis, Cornell University, Ithaca, NY.

Cuzzi, J. N., and R. H. Durisen 1990. Meteoroid bombardment of planetary rings: General formulation and effects of Oort cloud projectiles. *Icarus* **84**, 467–501.

Cuzzi, J. N., and P. R. Estrada 1998. Compositional evolution of Saturn's rings due to meteoroid bombardment. *Icarus* **132**, 1–35.

Cuzzi, J. N., J. J. Lissauer, L. W. Esposito, J. B. Holberg, E. A. Marouf, G. L. Tyler, and A. Boischot 1984. Saturn's rings: Properties and processes. In *Planetary Rings* (R. Greenberg and A. Brahic, Eds.), pp. 73–199. Univ. of Arizona Press, Tucson.

Cuzzi, J. N., R. C. French, L. Dones, P. R. Estrada, and M. R. Showalter 2000. Multicolor photometry of Saturn's main rings from HST and Voyager: Color variation with phase and opening angle, location, and optical depth. *Bull. Amer. Astron. Soc.* **32**, 1087.

Danielson, G. E., P. N. Kupferman, T. V. Johnson, and L. A. Soderblom 1981. Radiometric performance of the Voyager cameras. *J. Geophys. Res.* **86**, 8683–8689.

Domingue, D., and B. Hapke 1992. Disk-resolved photometric analysis of europan terrains. *Icarus* **99**, 70–81.

Dones, L. 1998. Planetary rings. In *Solar System Ices* (B. Schmitt, C. deBergh, and M. Festou, Eds.). Kluwer Academic, Dordrecht/Norwell, MA.

Dones, L., M. R. Showalter, and J. N. Cuzzi 1989. Simulations of light scattering in planetary rings. In *Dynamics of Astrophysical Disks* (J. Sellwood, Ed.), pp. 25–26. Cambridge Univ. Press, Cambridge, UK.

Dones, L., J. N. Cuzzi, and M. R. Showalter 1993. Voyager photometry of Saturn's A ring. *Icarus* **105**, 184–215.

Dones, L., M. Showalter, R. French, and J. Lissauer 1999. The perils of Pandora. *Bull. Amer. Astron. Soc.* **31**, 9.03.

Doyle, L. R., L. Dones, and J. N. Cuzzi 1989. Radiative transfer modeling of Saturn's outer B ring. *Icarus* **80**, 104–135.

Durisen, R. H., N. L. Cramer, B. W. Murphy, J. N. Cuzzi, T. L. Mullikin, and S. E. Cederbloom 1989. Ballistic transport in planetary ring systems due to particle erosion mechanisms. I: Theory, numerical methods, and illustrative examples. *Icarus* **80**, 136–166.

Durisen, R. H., P. W. Bode, J. N. Cuzzi, S. E. Cederbloom, and B. W. Murphy 1992. Ballistic transport in planetary ring systems due to particle erosion mechanisms. II: Theoretical models for Saturn's A- and B-ring inner edges. *Icarus* **100**, 364–393.

Epstein, E. E., M. A. Janssen, and J. N. Cuzzi 1984. Saturn's rings—3-mm low-inclination observations and derived properties. *Icarus* **58**, 403–411.

Esposito, L. W. 1987 Structure and evolution of Saturn's rings. *Icarus* **67**, 345–357.

Esposito, L. W., and K. Lumme 1977. The tilt effect for Saturn's rings. *Icarus* **31**, 157–167.

Esposito, L. W., J. N. Cuzzi, J. B. Holberg, E. A. Marouf, G. L. Tyler, and C. C. Porco 1984. Saturn's rings: Structure, dynamics, and particle properties. In *Saturn* (T. Gehrels and M. Matthews, Eds.). Univ. of Arizona Press, Tucson.

Estrada, P., and J. N. Cuzzi 1996. Voyager observations of the color of Saturn's rings. *Icarus* **122**, 251–272. [Also Erratum. *Icarus* **125**, 474.]

Fanale, F. P., and the Galileo NIMS, SSI, and UVIS instrument teams 1999. Galileo's multiinstrument spectral view of Europa's surface composition. *Icarus* **139**, 179–188.

Franklin, F. A., and A. F. Cook 1965. Optical properties of Saturn's rings. II: Two-color phase curves of the two bright rings. *Astron. J.* **70**, 704–720.

French, R. G., J. Cuzzi, R. Danos, L. Dones, and J. Lissauer 1998a. Hubble Space Telescope observations of spokes in Saturn's rings. In *Nantes Conference on Jupiter after Galileo and Saturn before Cassini, May 1998*.

French, R. G., D. Graham, J. Cuzzi, L. Dones, and J. Lissauer 1998b. Hubble Space Telescope observations of Saturn's rings: The opposition effect. *Bull. Amer. Astron. Soc.* **30**, 1045–1046.

French, R. G., K. J. Hall, C. A. McGhee, P. D. Nicholson, J. Cuzzi, L. Dones, and J. Lissauer 1998c. The Peregrinations of Prometheus. *Bull. Amer. Astron. Soc.* **30**, 1141.

French, R. G., C. A. McGhee, P. D. Nicholson, L. Dones, and J. Lissauer 1999. Saturn's wayward shepherds: Pandora and Prometheus. *Bull. Amer. Astron. Soc.* **31**, 9.01.

French, R. G., L. Dones, and H. Salo 2000. HST observations of the azimuthal brightness asymmetry in Saturn's rings. *Bull. Amer. Astron. Soc.* **32**, 8.02.

Geissler, P., W. R. Thompson, R. Greenberg, J. Moersch, A. McEwen, and C. Sagan 1995. Galileo multispectral imaging of Earth. *J. Geophys. Res.* **100**(E8), 16,895–16,906.

Geissler, P., C. Phillips, and T. Denk 1997. The color of Europa: Comparisons with Ganymede, Callisto, and Antarctica. In *Proceedings of Workshop on Remote Sensing of Planetary Ices: Earth and Other Solar System Bodies, Flagstaff, AZ, June 1997*.

Goertz, C. K., and G. E. Morfill 1983. A model for the formation of spokes in Saturn's rings. *Icarus* **53**, 219–229.

Goldreich, P., and S. Tremaine 1982. Dynamics of planetary rings. *Ann. Rev. Astron. Astrophys.* **20**, 249–283.

Gradie, J., and J. Veverka 1986. The wavelength dependence of phase coefficients. *Icarus* **66**, 455–467.

Grossman, A. 1990. Ph.D. thesis. California Institute of Technology, Pasadena.

Hapke, B., E. Wells, and J. Wagner 1981. Far-UV, visible, and near-IR reflectance spectra of frosts of H_2O, CO_2, NH_3, and SO_2. *Icarus* **47**, 361–367.

Hendrix, A. R. 1998. Galileo UVS observations of Europa: Variations of ultra-violet absorber with surface patterns. *EOS Trans.* **79**, F535.

Hendrix, A. R., C. A. Barth, C. W. Hord, and A. L. Lane 1998. Europa: Disk resolved ultraviolet measurements using the Galileo ultraviolet spectrometer. *Icarus* **135**, 79–94.

Holtzman, J. A., C. J. Burrows, S. Casertano, J. J. Hester, J. T. Trauger, A. M. Watson, and G. Worthey 1995. The photometric performance and calibration of WFPC2. *Publ. Astron. Soc. Pacific* **107**, 1065–1093.

Horn, L. J., and J. N. Cuzzi 1996. Characteristic wavelengths of irregular structure in Saturn's B and A rings. *Icarus* **119**, 285–310.

Jenniskens, P. 1993. Optical constants of organic refractory residue. *Astron. Astrophys.* **274**, 653–661.

Karkoschka, E. 1994. Spectrophotometry of the jovian planets and Titan at 300- to 1000-nm wavelength: The methane spectrum. *Icarus* **111**, 174–192.

Krist, J., and R. Hook 1999. *The Tiny Tim User's Guide*, version 5.0; available at http://www.wtsci.edu/software.

Lane, A. L., R. M. Nelson, and D. L. Matson 1981. Evidence for sulfur implantation in Europa's UV absorption band. *Nature* **292**, 38–39.

Lebofsky, L. A., T. V. Johnson, and T. B. McCord 1970. Saturn's rings: Spectral reflectivity and compositional implications. *Icarus* **13**, 226–230.

Lissauer, J. J., and J. N. Cuzzi 1985. Rings and moons—clues to understanding the solar nebula. In *Protostars and Planets* (D. Black and M. S. Matthews, Eds.), pp. 920–958. Univ. of Arizona Press, Tucson.

Lumme, K., and E. Bowell 1981. Radiative transfer in the surfaces of atmosphereless bodies. II: Interpretation of phase curves. *Astron. J.* **86**, 1705–1721.

Lumme, K., and W. M. Irvine 1976. Photometry of Saturn's rings. *Astron. J.* **81**, 865–893.

Lumme, K., W. M. Irvine, and L. W. Esposito 1983. Theoretical interpretation for the tilt effect of Saturn's rings. *Icarus* **53**, 174–184.

McLure, R. J., J. S. Dunlop, and M. J. Kukula 2000. Two-dimensional modelling of the optical HST and infrared tip-tilt images of quasar host galaxies. *Mon. Not. R. Astron. Soc.* **318**, 693–702.

Morfill, G. E., H. Fechtig, E. Grün, and C. K. Goertz 1983. Some consequences of meteoroid impacts on Saturn's rings. *Icarus* **55**, 439–447.

Morris, R. V., and D. C. Golden 1998. Goldenrod pigments and the occurrence of Hematite and possibly Goethite in the Olympus–Amazonis Region of Mars. *Icarus* **134**, 1–10.

Nicholson, P. D., M. R. Showalter, L. Dones, R. G. French, S. M. Larson, J. J. Lissauer, C. A. McGhee, P. Seitzer, B. Sicardy, and G. E. Danielson 1996. Observations of Saturn's ring-plane crossings in August and November 1995. *Science* **272**, 509–515.

Nicholson, P. D., R. G. French, J. N. Cuzzi, K. Matthews, O. Perković, R. J. Stover, E. Tollestrup, and J. Harrington 2000. Saturn's rings I: Optical depth profiles from the 28 Sgr occultation. *Icarus* **145**, 474–501.

Noland, M., J. Veverka, D. Morrison, D. P. Cruikshank, A. R. Lazarewicz, N. D. Morrison, J. L. Elliot, J. Goguen, and J. A. Burns 1974. Six-color photometry of Iapetus, Titan, Rhea, Dione, and Tethys. *Icarus* **23**, 334–354.

Noll, K. S., H. A. Weaver, and A. M. Gonnella 1995. The albedo spectrum of Europa from 2200 Å to 3300 Å. *J. Geophys. Res.* **100**(E9), 19,057–19,059.

Noll, K. S., R. E. Johnson, A. L. Lane, D. L. Domingue, and H. A. Weaver 1996. Detection of ozone on Ganymede. *Science* **273**, 341–343.

Noll, K. S., T. L. Roush, D. P. Cruikshank, R. E. Johnson, and Y. J. Pendleton 1997. Detection of ozone on Saturn's satellites Rhea and Dione. *Nature* **388**, 45–47.

Ockert, M. E., R. M. Nelson, A. L. Lane, and D. L. Matson 1987. Europa's ultraviolet absorption band (260–320 nm): Temporal and spatial evidence from IUE. *Icarus* **70**, 499–505.

Oke, J. B. 1990. Faint spectrophotometric standard stars. *Astron. J.* **99**, 1621–1631.

Pollack, J. B. 1974. The rings of Saturn. *Space Sci. Rev.* **18**, 3–93.

Pollack, J. B., A. Summers, and B. Baldwin 1973. Saturn's rings: Particle sizes and cosmogonic implications. *Icarus* **20**, 263–278.

Porco, C. C., H. R. Throop, and D. C. Richardson 2001. Light scattering in Saturn's rings: Basic disk properties and the A ring Azimuthal Asymmetry. *Bull. Amer. Astron. Soc.* **33**, 1091.

Poulet, F., E. Karkoschka, and B. Sicardy 1999. Spectrophotometry of Saturn's small satellites and rings from Hubble Space Telescope images. *J. Geophys. Res.* **104**(E10), 24,095–24,110.

Poulet, F., J. N. Cuzzi, and L. Dones 2000. *Modeling the Phase Variation of Saturn's Ring Brightness and Color from HST Observations*. DPS, Pasadena.

Poulet, F., J. N. Cuzzi, R. G. French, and L. Dones 2002. A study of Saturn's ring phase curves from HST observations. *Icarus* **158**, 224–248.

Richardson, D. R. 1994. Tree code simulations of planetary rings. *Mon. Not. R. Astron. Soc.* **269**, 493–511.

Salo, H. 1992. Gravitational wakes in Saturn's rings. *Nature* **359**, 619–621.

Salo, H. 1995. Simulations of dense planetary rings. III. Self-gravitating identical particles. *Icarus* **117**, 287–312.

Salo, H., and R. Karjalainen 2001. *Photometric Modeling of Saturn's Rings: I. Monte Carlo Method and the Effect of Nonzero Filling Factor*, Icarus, submitted for publication.

Salo, H., R. Karjalainen, and R. G. French 2000. Modeling the azimuthal brightness asymmetry in Saturn's rings. *Bull. Amer. Astron. Soc.* **32**, #08.01.

Showalter, M. 1998. Detection of cm-sized meteoroid impact events in Saturn's F ring. *Science* **282**, 1099–1102.

Simonelli, D., and J. Veverka 1986. Disk-resolved photometry of Io; II: Opposition surges and normal reflectances. *Icarus* **66**, 428–454.

Smith, B. A., L. Soderblom, J. Beebe, G. Briggs, A. Bunker, S. A. Collins, C. Hansen, T. Johnson, J. Mitchell, R. Terrile, M. Carr, A. Cook, J. Cuzzi, J. Pollack, G. E. Danielson, A. Ingersoll, M. Davies, G. Hunt, H. Masursky, E. Shoemaker, D. Morrison, T. Owen, C. Sagan, J. Veverka, R. Strom, and V. Suomi, 1981. Encounter with Saturn: Voyager 1 imaging results. *Science* **212**, 163–191.

Stern, S. A., L. M. Trafton, and B. Flynn 1995. Rotationally resolved studies of the mid-UV spectrum of Triton. II: HST surface and atmospheric results. *Astron. J.* **109**, 2855–2868.

Trafton, L. M., and S. A. Stern 1996. Rotationally resolved spectral studies of Pluto from 2500 to 4800 Å obtained with HST. *Astron. J.* **112**, 1212–1224.

Trauger, J. T., R. W. Vaughan, R. W. Evans, and D. C. Moody 1996. Geometry of the WFPC2 focal plane. In *Calibrating Hubble Space Telescope: Post Servicing Mission* (A. Koratkar and C. Leitherer, Eds.), pp. 171–193. Space Telescope Science Institute, Baltimore.

Verbiscer, A., and P. Helfenstein 1998. Reflectance spectroscopy of icy surfaces. In *Solar System Ices* (B. Schmitt, C. deBergh, and M. Festou, Eds.), pp. 157–197. Kluwer Academic, Dordrecht/Norwell, MA.

Wagener, R., and J. J. Caldwell 1986. IUE observations of Saturn's rings. In *New Insights in Astrophysics: 8 Years of Astronomy with IUE*. ESA SP-263.

Wagener, R., and J. J. Caldwell 1988. On the abundance of micron-sized particles in Saturn's A and B rings. In *A Decade of Astronomy with the IUE Satellite*, ESA SP-281.